

Direct power spectral density estimation from structure functions without Fourier transforms

Mark A. Bishop,^{1, a)} Sean Oughton,² Tulasi N. Parashar,¹ and Yvette C. Perrott¹

¹⁾*School of Chemical and Physical Sciences, Victoria University of Wellington, Wellington 6012, New Zealand*

²⁾*Department of Mathematics, University of Waikato, Hamilton 3240, New Zealand*

(Dated: 4 February 2026)

Second-order structure functions and power spectral densities are popular tools in the study of statistical properties across scales, particularly for the analysis of turbulent flows. Although intimately related, analyses primarily use one or the other. We introduce a framework for estimating the power spectrum using the second-order structure function without applying Fourier transforms – enabling one to take advantage of the real-space structure function calculations. We validate and showcase this method, comparing it to classical Fourier power spectrum estimates determined from analytical calculations, fractional Brownian motion, turbulence simulations, and space-physics and astrophysical observations of turbulence. We show that this method is able to robustly obtain the expected power law behaviour where we use turbulence ranges as test-cases.

^{a)}Electronic mail: mark.bishop@vuw.ac.nz

I. INTRODUCTION

In the analysis of complex physical systems – particularly those exhibiting turbulent, fractal, or stochastic behaviour – two key statistical tools are frequently employed: the power spectral density (PSD, which we will use interchangeably with power spectrum and spectrum) and the second order structure function (SF).

The power spectral density characterizes how the power (or variance) of a signal is distributed over some notion of *scale* – wavenumber or frequency. Power spectra are defined and often estimated through Fourier transform methods¹. These methods come in many variations, *e.g.*, the periodogram², Blackman-Tukey³, Welch’s method, and the Lomb-Scargle periodogram⁴, *etc.* These classical/non-parametric methods have been developed over decades and have their respective advantages, disadvantages, and use-cases depending on the behaviour of the data that are being examined^{5–7}. Some of these use-cases refer to gapped or non-uniformly sampled data which breaks the classic Nyquist aliasing relation and leads to degraded performance on spectral estimation⁸. Vast amounts of research has been performed in comparing and quantifying the influences of gapped and non-uniformly sampled data for different methods of PSD estimation through *e.g.*, interpolation of the data in gaps, or window/tapering the data^{9–14}.

Alternatively, the structure function – specifically, the second-order structure function – measures the average squared difference between the signal at two points separated by a given lag. This lag separation is also some notion of *scale* – in the time or spatial domain. The structure function is often estimated directly from the observed data where lag separations are available *i.e.*, values are based off pairs in the data, so if one or both values in a pair are missing, it can simply be ignored^{15–19}.

Though PSDs and SFs operate in different domains (frequency/wavenumber versus time/space), under assumptions of stationarity the SF is mathematically related to the PSD by an integration of the PSD^{20–23}. In the case of a stationary, homogeneous process with a PSD that has a range of wavenumbers that is a power-law $\mathcal{E}_D(k) \propto k^{-\beta}$, the second-order SF $\bar{S}_D(\ell) \propto \ell^\eta$ is expected to scale with $\eta = \beta - 1$ within specific bounds $1 < \beta < 3$.

In turbulence studies power-law scaling is a key signature of energy cascades for both the PSD²⁴ and the SF²⁵. The spectral slopes in either domain have been used to estimate the turbulent kinetic energy dissipation rates across various environments including the

ocean^{26,27}, the atmosphere²⁸, and chemical processes²⁹. The power-law scaling has been used to understand the role turbulence plays in promoting and inhibiting star-formation in the interstellar medium with both the PSD and SF providing complementary statistics about energy cascades via spectral slopes, and transitional scales via changes in slopes^{30–34}.

Since the earliest of space missions, the PSD and SF spectral estimates have been used to measure the properties of turbulence in the solar wind^{35,36}, a “laboratory” for plasma turbulence experiments^{37–44}. This is an astrophysical context that often provides *in-situ* measurements, typically as 1-dimensional time-series data. SFs are frequently employed to mitigate the effect of data gaps and telemetry dropouts with accurate spectral estimation claimed for missing fractions of up to 68%^{45–47}. Some work has shown that the SF is susceptible to missing data^{23,48}, but it has been suggested that this can be mitigated using empirically derived correction factors⁴⁹.

Beyond solar wind studies, two-dimensional telescope observations of line emissions of the interstellar and intracluster mediums are used to infer the velocity structure of astrophysical fluids^{50,51}. However, these images often consist of irregularly shaped or non-uniformly distributed binned pixels, which makes traditional Fourier-based PSD estimation difficult. Therefore, SF analysis is often used^{19,52,53}.

Similarly, in two-dimensional X-ray observations of the intracluster medium, the surface brightness maps often contain gaps caused by observational constraints or the removal of contaminating sources such as galaxies^{54–56}. These gaps introduce aliasing artifacts in Fourier PSD estimates, prompting the use of spatial-domain techniques^{57–60}. Full spectral characterization can still be useful as correcting for instrumental or observational noise is often done in Fourier space⁵⁴ whereas uncertainties are better understood in the spatial domain^{23,61,62}.

In this paper, we discuss a method for directly estimating the power spectrum using second-order structure functions. Practically speaking, this method uses lag-space computations, which can be advantageous when Fourier-space computations may introduce aliasing problems^{60,63,64}.

Previous studies have used approximate variants of this approach, including in the analysis of solar wind time-series data^{65–68} and laboratory turbulence experiments^{69,70}. Our work extends these efforts by using a more rigorous derivation^{68,71}, including corrections for systematic biases that were previously unrecognized. Additionally, we provide a de-

tailed investigation of the mathematical relationship between the lag distance and Fourier wavenumber and provide extensions of common values to arbitrary dimension.

The remainder of this paper starts with detailing the calculations required to obtain the SF to PSD relation (Section II). Next, Section III discusses the biases and factors associated with approximating the PSD with the structure function. This is accomplished through analytical work and examples with additional analytical work in Appendix A. Section IV introduces details regarding the practical implementation of, and validates the performance on fractional Brownian motion (fBm) fields with comparison to the analytical scenarios of the previous section. Finally, Section V showcases the method with high-resolution real-world datasets/observations.

II. METHOD

This section outlines the approach we take to obtain an *equivalent spectrum*, by which we mean a quantity calculated using structure functions (or similar quantities) that—without use of a Fourier transform—can be interpreted as an approximation to the actual spectrum. Similar approaches and formulae have been presented previously^{68,69,71–73}.

We begin by considering a zero-mean scalar field, $s_D(\mathbf{x})$, for which measurements are available in a Euclidean space of dimension D , with $\mathbf{x} \in \mathbb{R}^D$ the vector of spatial coordinates. An important distinction here is that D is not necessarily the dimension of the system itself (D_s , say). Indeed, the latter will often be larger than D since measurement techniques are frequently restricted to 1D or 2D samples of 3D systems. We assume that the statistics (e.g., moments) of $s_D((\mathbf{x}))$ are homogeneous.

Recall that the angle-averaged second-order structure function,

$$\overline{S}_D(\ell) = \langle |s_D(\mathbf{x} + \boldsymbol{\ell}) - s_D(\mathbf{x})|^2 \rangle, \quad (1)$$

is related to the angle-averaged autocorrelation function,

$$\overline{R}_D(\ell) = \langle s_D(\mathbf{x})s_D(\mathbf{x} + \boldsymbol{\ell}) \rangle, \quad (2)$$

by the standard result

$$\overline{S}_D(\ell) = 2\overline{R}_D(0) - 2\overline{R}_D(\ell), \quad (3)$$

where the overbar and $\langle \cdot \rangle$ indicate averaging over two things: position \mathbf{x} , and the direction of the lag vector ℓ for fixed magnitude ℓ . Homogeneity means that quantities so averaged do not depend on the (absolute) positions \mathbf{x} .

Letting $\ell \rightarrow \infty$, we have

$$\bar{S}_D(\infty) = 2\bar{R}_D(0) = 2\langle s_D(\mathbf{x})^2 \rangle, \quad (4)$$

since $\lim_{\ell \rightarrow \infty} \bar{R}_D(\ell) = 0$. As this is essentially the ‘energy’ associated with s_D , we may make use of Parseval’s theorem to relate it to the (Fourier space) integral of an angle-integrated energy spectrum, $\mathcal{E}_D(k)$,

$$\bar{S}_D(\infty) = 2 \int_0^\infty \mathcal{E}_D(k) dk = \int_0^\infty \frac{d\bar{S}_D(\ell)}{d\ell} d\ell, \quad (5)$$

where the rightmost form follows from the fundamental theorem of calculus and $\bar{S}_D(0) = 0$. The definition of $\mathcal{E}_D(k)$ —the angle-integrated spectrum available when the measurement space dimension is D —is important and will be discussed shortly.

Introducing the equivalent wavenumber⁷⁴

$$k_e = \frac{b}{\ell}, \quad (6)$$

where b is a conversion factor to be defined later, and using it to make a change of variable in Equation 5 yields

$$\int_0^\infty \frac{\ell^2}{b} \frac{d\bar{S}_D(\ell)}{d\ell} dk_e = 2 \int_0^\infty \mathcal{E}_D(k) dk. \quad (7)$$

Equation 7 is exact, although of course it does not mean that the integrands are equal. Nonetheless, we now assume that there may be some scale range(s) over which the integrands are approximately equal, and define the *equivalent spectrum* by,

$$\tilde{\mathcal{E}}_D^S(k_e) = \frac{1}{2} \frac{1}{b} \ell^2 \frac{d\bar{S}_D(\ell)}{d\ell} \bigg|_{\ell=b/k_e}. \quad (8)$$

When the near equality of the integrands is good, we will then have

$$\tilde{\mathcal{E}}_D^S(k_e) \approx \mathcal{B} \mathcal{E}_D(k_e), \quad (9)$$

where the bias \mathcal{B} is discussed below. The relationship to *signature functions*⁷⁵ is discussed in Section C.

To reiterate: for homogeneous turbulence Equation 7 is exact—however, it of course does *not* mean that the integrands (used in inferring Equation 8) are pointwise equal. For example, the following definite integrals are equal: $\int_0^1 x \, dx = \frac{1}{2} \int_0^1 \, dx$ and yet their integrands are not. Nonetheless we will demonstrate there are circumstances under which there is an equivalence/proportionality of the integrands, at least for some range of k_e . These circumstances are explored analytically in Section III and empirically validated in Section IV, making use of several model spectra that are relevant to turbulence problems. As we shall see, that analysis indicates that the methodology can be useful in various applications. However, care is needed. As b and \mathcal{B} typically vary with the application, we urge readers to individually examine the systematic biases for their specific use-cases.

As a technical matter, $\tilde{\mathcal{E}}_D^S(k_e)$ is a *biased* estimator that approximates the actual spectrum $\mathcal{E}_D(k)$ by allowing for a possible deviation in amplitude by the factor \mathcal{B} and a possible shift of the wavenumber argument. Determining suitable values for \mathcal{B} and b is a key step in obtaining a useful and accurate equivalent spectrum and these factors are discussed in detail in the next section.

Let us return to the definition of $\mathcal{E}_D(k)$. We will need to distinguish between several types of spectra: modal, angle-averaged, and reduced. See Appendix B 1 for definitions. (Note that when $D = 3$ some works call the angle-averaged spectra the 3D spectrum^{75,76}. Herein, we will use the less ambiguous terms angle-averaged or omni-directional.) Suppose that we have access to realizations of the full continuum of values of $s_D(\mathbf{x})$ in the D -dimensional space in which measurements occur (e.g., $D = 2$ because of line-of-sight integration, or $D = 1$ for observations made by a spacecraft). Using these realizations, one can construct the correlation function for all lags $\boldsymbol{\ell}$ and Fourier transform it to obtain a modal spectrum, $E_D(\mathbf{k}_D)$; see Equation B1. Employing appropriate polar coordinates, this can be integrated over the $D - 1$ angles to get the $\mathcal{E}_D(k)$ that appears in Equation 5–Equation 9. It is this quantity that the equivalent spectrum is an approximation to.

Frequently, the measurements will be made in 1D or 2D, while the system itself will be 3D. For those situations, the modal and angle-integrated spectra for the *system* will differ from the spectra $E_D(\mathbf{k}_D)$ and $\mathcal{E}_D(k)$ obtainable from the measurement dataset. Examples are given in Appendix B 2. Moreover, as is well known, except in special cases (e.g., high symmetry), it is not usually possible to obtain the angle-integrated spectrum associated with the full system, $\mathcal{E}^{\text{sys}}(k)$, say, from $\mathcal{E}_D(k)$.

Note also that the definitions and formulae provided here are also valid when $s_D(\mathbf{x})$ is replaced by a vector field $\mathbf{v}_D(\mathbf{x})$, in which case the absolute value becomes the vector norm and the scalar multiplication in Equation 2 becomes the Euclidean dot product.

III. AMPLITUDE \mathcal{B} & WAVENUMBER b BIAS

Equation 6 and Equation 8 have introduced somewhat arbitrary factors (\mathcal{B} and b) that can be thought of as corresponding to an amplitude bias (\mathcal{B}) and wavenumber bias (b). Here, bias is used to mean a systematic correction is needed. The amplitude bias is associated with correcting the “power” of $\tilde{\mathcal{E}}_D^S(k_e)$ and will often be considered as the ratio of the genuine Fourier spectrum $\mathcal{E}_D(k)$ to the structure function based estimate $\tilde{\mathcal{E}}_D^S(k_e)$. The wavenumber bias is associated with converting the lag-scale ℓ to the Fourier wavenumber k .

This section describes the process for investigating the appropriate amplitude factor \mathcal{B} and wavenumber factor b which could be used in future work, and developed further for specific use cases. We propose formulae and approximations for \mathcal{B} and b that result in adequate estimations for most turbulence spectra. These formulae should be applicable for many other scale-dependent phenomena assuming their spectra are similar to the ones we model.

For reference, Table I provides a list of symbols and their definitions used throughout this paper.

A. Pure Power Law Spectrum

As has been extensively discussed in the literature, a relationship between the structure function and the amplitudes of the power spectrum can be calculated for pure power law spectra^{21,22}. Our equivalent spectrum approach also has a bias \mathcal{B} which is readily calculated for a pure power law. Using the following pure power law spectrum with $1 < \beta < 3$,

$$\mathcal{E}_D(k) = Ak^{-\beta}, \quad (10)$$

we can calculate the structure function using its exact spectral representation^{20,23},

$$\overline{S}_D(\ell) = 2 \int_0^\infty [1 - \mathcal{T}_D(k\ell)] \mathcal{E}_D(k) dk, \quad (11)$$

Name	Symbol	Definition(s)
Angle-averaged second-order structure function	$\bar{S}_D(\ell)$	Equation 1, Equation 11
Angle-averaged autocorrelation function	$\bar{R}_D(\ell)$	Equation 2
Angle-integrated spectrum	$\mathcal{E}_D(k)$	Equation 5, Equation 17a
Equivalent wavenumber	k_e	Equation 6
Amplitude bias correction factor	\mathcal{B}	Section III
Wavenumber bias correction factor	b	Section III
Equivalent spectrum	$\tilde{\mathcal{E}}_D^S(k_e)$	Equation 8, Equation 18a, Equation 23
Equivalent spectrum (power law approx.)	$\tilde{\mathcal{P}}_D^S(k_e)$	Equation 32
Local power law slope for $\tilde{\mathcal{E}}_D^S(k_e)$	$\Delta\tilde{\beta}(k_e)$	Equation 31
Effective energy-containing scale for $\mathcal{E}_D(k)$	k_p	Equation 15a
Effective energy-containing scale for $\tilde{\mathcal{E}}_D^S(k_e)$	$k_{e,p}$	Equation 15b
Estimated b factor at k_p	$b_{p,D}^{\text{est}}$	Equation 27
Empirical b factor at k_p	$b_{p,D}^{\text{emp}}$	Equation 30
Analytical bias for a pure power law function	B_D^{pow}	Equation 12
Analytical bias for the exp. model spectrum	B_D^{exp}	Equation 29
Analytical bias for the exp. model using $\tilde{\mathcal{P}}_D^S(k_e)$	$\tilde{B}_D^{\text{exp-pow}}$	Equation 33

TABLE I. **Table of frequently used symbols in this paper.**

where $\mathcal{T}_D(k\ell)$ is given by Equation B5.

The equivalent spectrum corresponding to the pure power-law $\mathcal{E}_D(k)$ is analytically evaluated using Equation 11 as

$$\tilde{\mathcal{E}}_D^S(k_e) = \underbrace{\left(\frac{2}{b}\right)^{1-\beta} \frac{\Gamma\left(\frac{D}{2}\right) \Gamma\left(\frac{3-\beta}{2}\right)}{\Gamma\left(\frac{\beta+D-1}{2}\right)}}_{B_D^{\text{pow}}} \underbrace{\left[Ak_e^{-\beta}\right]}_{\mathcal{E}_D(k_e)}. \quad (12)$$

As indicated by the square brackets, clearly $\tilde{\mathcal{E}}_D^S(k_e)$ contains $\mathcal{E}_D(k = k_e)$. However, there exist additional coefficients that depend on b , D , and β . These coefficients (denoted B_D^{pow} in Equation 12) form a natural bias in the spectral estimation *i.e.*, $\tilde{\mathcal{E}}_D^S(k_e)$ has a different amplitude than $\mathcal{E}_D(k = k_e)$. Such amplitude biases have previously been investigated in the *signature function* literature^{72,75} (see, Appendix C for more details).

We now emphasize two scenarios that can be deduced from the above equations:

- **b is a function of the spectral index β .**

We could determine a b to equate Equation 12 to Equation 10, *i.e.*, $B_D^{\text{pow}}(\beta, b) = 1$ implies

$$b = b_D^{\text{pow}}(\beta) \equiv 2 \left[\frac{\Gamma\left(\frac{D}{2}\right) \Gamma\left(\frac{3-\beta}{2}\right)}{\Gamma\left(\frac{\beta+D-1}{2}\right)} \right]^{1/(1-\beta)}. \quad (13)$$

We can clearly see that the value of b needed to equate Equation 12 to Equation 10 changes with β and D (see the $B_D^{\text{pow}}(\beta, b) = 1$ contour in Figure 1) – the source of this result is discussed in Section III C.

If we were to choose a b dependent on the power law index β we would complicate the relationship between a wavenumber k and lag distance ℓ . Not to mention, practically determining b would require *a priori* spectral slope knowledge.

In this case, *there is no universal b .*

- **b is a constant.**

It would be more natural to fix $b = \text{const.}$ to obtain a physically motivated relationship $k_e = b/\ell$ describing the connection between the Fourier wavenumber and a real-space (lag) scale.

Equivalence of Equation 12 and Equation 10 requires that

$$\mathcal{B} = B_D^{\text{pow}}(\beta, b) \equiv \left(\frac{2}{b} \right)^{1-\beta} \frac{\Gamma\left(\frac{D}{2}\right) \Gamma\left(\frac{3-\beta}{2}\right)}{\Gamma\left(\frac{\beta+D-1}{2}\right)}. \quad (14)$$

In Figure 1, we display a visualization of Equation 14 showing how the bias factor $B_D^{\text{pow}}(\beta, b)$ behaves as a function of b and β for $D = 1, 2, 3$. In other words, b does not influence the spectral power-law – it is possible to obtain the correct power-law slope for any reasonable, constant choice of b . Any discrepancy between the chosen b and Equation 13 is simply absorbed into the systematic bias Equation 14. However, with different values employed in the literature, unfortunately, a constant b factor is a great source of ambiguity – with values of 1, π , or 2π commonly used^{34,68,71,72,75,77}. This ambiguity is highlighted in the next section.

For now, if we assert $b = 1$, then as Figure 2 shows, B_D^{pow} is low (for $D = 2, 3$) to modest (for $D = 1$) for reasonable β values (*e.g.*, Kolmogorov $\beta \approx 5/3$). This explains some of the success in previous solar wind ($D = 1$) analyses^{67,68} which effectively applied

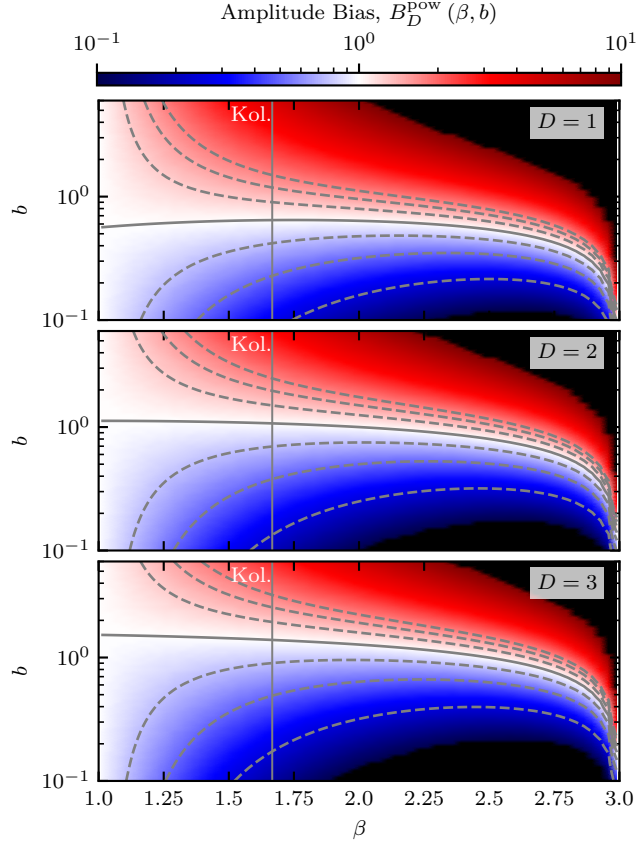


FIG. 1. The amplitude bias Equation 14 for a pure power law angle-integrated spectrum Equation 10, for Euclidean dimensions $D = 1$, $D = 2$, and $D = 3$. The line contours correspond to linear spacings of 0.25 starting from $B_D^{\text{pow}} = 0.25$ to 1.75 with $B_D^{\text{pow}} = 1$ represented by the solid gray line. The solid vertical gray line represents the (Kolmogorov) power law slope of 5/3.

$\tilde{\mathcal{E}}_D^S(k_e)$ with $b = 1$ (see Appendix B 2 for further details). Also notable, is the bias for $D = 2$: it is close to unity for $1 < \beta \lesssim 2$ (*i.e.*, nearly no bias), suggesting that this is an effective method for estimating power spectral densities of observations of turbulence (telescope images) in astrophysical plasmas such as the intracluster medium (ICM) of galaxy clusters⁷⁸, and the interstellar medium (ISM)⁵¹. However, we note that telescope images are 2-dimensional projections of 3-dimensional physical structures, and therefore do not correspond to truly $D = 2$ measurements (see Appendix B 2 for further details). We leave the impact of the projection to future work.

For steep spectra (large β), B_D^{pow} is large and so $\tilde{\mathcal{E}}_D^S(k_e)$ becomes a worse estimate – consistent with the *signature function* literature (see, Appendix C).

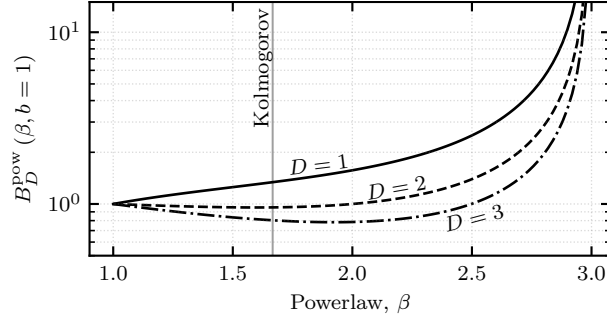


FIG. 2. The amplitude bias Equation 14 with fixed $b = 1$ for a pure power law angle-integrated spectrum Equation 10, for Euclidean dimensions $D = 1$ (dashed), $D = 2$ (dotted), and $D = 3$ (dash-dotted). The solid vertical gray line represents the (Kolmogorov) power law slope of $-5/3$.

Since a β dependent b argument seems impractical for analysis of real observations, from here on we focus on the case of a constant b , and explore *which* value of b is most appropriate under some example circumstances along with the amplitude biases induced and how to correct for them.

B. Analytical Solutions of Model Correlation Functions

Unbounded pure power law spectra are not physical, and regions of pure power law do not even necessarily indicate turbulent behaviour. In addition, we are also left with ambiguity in a constant b . We therefore consider a more nuanced approach where we attempt to determine appropriate choices of b by focusing on the location of the peaks of $\mathcal{E}_D(k)$ and $\tilde{\mathcal{E}}_D^S(k_e)$ by modelling spectra that are *not* pure-power law functions. The peaks of the associated spectra are at the wavenumbers

$$k_p = \operatorname{argmax}_k \{\mathcal{E}_D(k)\}, \quad (15a)$$

$$k_{e,p} = \operatorname{argmax}_{k_e} \{\tilde{\mathcal{E}}_D^S(k_e)\}, \quad (15b)$$

where k_p and $k_{e,p}$ can be thought of as an effective energy-containing scale characteristic of the turbulence energy-containing/outer scales (*e.g.*, injection scale, correlation scale, *etc*)²².

From Section III A we already know the pure power-law behaviour is well captured by $\tilde{\mathcal{E}}_D^S(k_e)$. However, if we wish to accurately approximate the PSD using the equivalent SF, it should also accurately describe an energy-containing scale L . We investigate model spectra

with a distinctive scale range in $\mathcal{E}_D(k)$ associated with the $L \sim 1/k_p$ that transitions to a pure power law regime at $k \gg 1/L$.

We will use the following model,

$$\bar{R}_D(\ell) = D e^{-\ell/L}, \quad (16)$$

where L corresponds to some energy-containing scale (in this case, the correlation length). This is a case already present in the literature for Hurst parameter $H = 1/2$, but we have extended to arbitrary dimensions D^{22} .

The corresponding angle-integrated spectrum is^{1,57}

$$\mathcal{E}_D(k) = \frac{\Omega_D^2}{(2\pi)^D} \int_0^\infty \bar{R}_D(\ell) \mathcal{T}_D(k\ell) (k\ell)^{D-1} d\ell, \quad (17a)$$

$$= \frac{2}{\sqrt{\pi}} \frac{DL^D k^{D-1}}{(L^2 k^2 + 1)^{(D+1)/2}} \frac{\Gamma(\frac{D+1}{2})}{\Gamma(\frac{D}{2})}, \quad (17b)$$

$$= \begin{cases} \frac{2}{\pi} \frac{L}{1+L^2 k^2}, & D = 1 \\ \frac{2L^2 k}{(1+L^2 k^2)^{3/2}}, & D = 2 \\ \frac{12}{\pi} \frac{L^3 k^2}{(1+L^2 k^2)^2}, & D = 3 \\ \dots, \end{cases} \quad (17c)$$

Using Equation 3 with Equation 8, the equivalent spectrum is

$$\tilde{\mathcal{E}}_D^S(k_e) = -\frac{\ell^2}{b} \frac{d\bar{R}_D(\ell)}{d\ell}, \quad (18a)$$

$$= b \frac{D}{L k_e^2} e^{-\frac{b}{L k_e}}. \quad (18b)$$

Equation 17b and Equation 18b have local power law behaviour as

$$\Delta\beta(k) = -\frac{d \ln(\mathcal{E}_D(k))}{d \ln(k)} = -\frac{D-1-2L^2 k^2}{1+L^2 k^2}, \quad (19)$$

$$\Delta\tilde{\beta}(k_e) = -\frac{d \ln(\tilde{\mathcal{E}}_D^S(k_e))}{d \ln(k_e)} = -\frac{b}{L k_e} + 2. \quad (20)$$

$\mathcal{E}_D(k)$ and $\tilde{\mathcal{E}}_D^S(k_e)$ follow the same power law slope for $kL, k_e L \gg 1$ *i.e.*, $\mathcal{E}_D(k) \sim k^{-2}$, $\tilde{\mathcal{E}}_D^S(k_e) \sim k_e^{-2}$. See Appendix A for an analytical case where $\tilde{\mathcal{E}}_{D=1}^S(k_e)$ has the correct power law behaviour for general power law β .

The effective energy-containing scales ($k_p, k_{e,p}$) of Equation 17b and Equation 18b are found using $\Delta\beta(k_p) = \Delta\tilde{\beta}(k_{e,p}) = 0$, which are

$$k_p = \frac{\sqrt{2D-2}}{2L} = \begin{cases} 0, & D = 1 \\ \frac{1}{\sqrt{2}} \frac{1}{L}, & D = 2 \\ \frac{1}{L}, & D = 3 \\ \dots \end{cases}, \quad (21)$$

$$k_{e,p} = \frac{b}{2L}. \quad (22)$$

This naturally provides the relationship $b = \sqrt{2D-2}$ for $D > 1$ which ensures that the peaks of Equation 17b and Equation 18b are aligned. This does not imply the amplitudes at the peaks are equal *i.e.*, $\mathcal{E}_D(k_p) \neq \tilde{\mathcal{E}}_D^S(k_{e,p})$. We merely choose a b so that the peaks of the respective spectra are located at the same wavenumber ($k_p = k_{e,p}$). Note, the case for $D = 1$ provides $b = 0$ because the peak of Equation 17b is at $k = 0$.

Unfortunately, this method of estimating an appropriate *constant* b is dependent on the underlying model of $\bar{R}_D(\ell)$. Table II shows some analytical expressions using different forms of $\bar{R}_D(\ell)$. Note, the third row in Table II is analogous to the model eddy of a swirling fluid of characteristic size L for $D = 3$ (Townsend's model)^{75,79}. The model correlation functions and spectra in Table II may serve as adequate models to verify some spectral estimate behaviours. We also note that some of the models in Table II result in non-positive $\tilde{\mathcal{E}}_D^S(k_e)$ for a range of $k_e \ll 1/L$. In these cases, $\tilde{\mathcal{E}}_D^S(k_e)$ would not be an appropriate approximation of $\mathcal{E}_D(k)$ within that negative region (since $\mathcal{E}_D(k)$ is a non-negative function *i.e.*, $\mathcal{E}_D(k) \geq 0$). Similar analysis have also been applied to the *signature functions* (for $D = 3$) to examine their validity for representing the turbulence energy-containing range⁷⁵ (see, Appendix C for more details).

It has been noted in previous work that local features in the PSD are non-local in the SF (see Equation 11) and the transfer of these local features from one space to the other is dependent on the functional form of the PSD^{75,80}. It would appear that the equivalent spectrum inherits this property – which we discuss in the next section. Consequently, when the constant b equates the energy-containing scales, its value depends on the functional form of the PSD. Therefore, *there is no universal constant b*.

$\frac{\bar{R}_D(\ell)}{A}$	$\frac{\mathcal{E}_D(k)}{A}$	$\frac{\tilde{\mathcal{E}}_D^S(k_e)}{A}$	k_p	$\frac{k_{e,p}}{b}$	$b \left[\equiv \frac{\ell}{D} \right]$
$De^{-\ell/L}$	$2DL^D k^{D-1} (L^2 k^2 + 1)^{-(D+1)/2} \frac{\Gamma(\frac{D+1}{2})}{\sqrt{\pi} \Gamma(\frac{D}{2})}$	$D b \frac{e^{-b/L k_e}}{L k_e^2}$	$\frac{\sqrt{2D-2}}{2L}$	$\frac{1}{2L}$	$\sqrt{2D}$
$\frac{(DL-\ell) e^{-\ell/L}}{L}$	$4L^{D+2} k^{D+1} (L^2 k^2 + 1)^{-(D+3)/2} \frac{\Gamma(\frac{D+3}{2})}{\sqrt{\pi} \Gamma(\frac{D}{2})}$	$b \left(DL + L - \frac{b}{k_e} \right) \frac{e^{-b/L k_e}}{L^2 k_e^2}$	$\frac{\sqrt{2D+2}}{2L}$	$\frac{\left(D \pm \sqrt{D^2+8} + 4 \right)}{4L(D+1)}$	$\frac{2\sqrt{2}(D+2)}{D+\sqrt{D^2+2}}$
$\frac{(DL^2 - 2\ell^2) e^{-\ell^2/L^2}}{L^2}$	$\frac{2^{-D}}{\Gamma(\frac{D}{2})} L^{D+2} k^{D+1} e^{-L^2 k^2/4}$	$2b^2 \left(DL^2 + 2L^2 - \frac{2b^2}{k_e^2} \right) \frac{e^{-b^2/L^2 k_e^2}}{L^4 k_e^3}$	$\frac{\sqrt{2D+2}}{L}$	$\frac{\sqrt{3D \pm 3\sqrt{D^2+2D+25} + 21}}{3L\sqrt{D+2}}$	$\frac{\sqrt{6D^2+1}}{\sqrt{D+\sqrt{D^2+2}}}$

TABLE II. **Analytical solutions for spectra using different model autocorrelation functions.** Shown is: the angle-integrated spectrum $\mathcal{E}_D(k)$ and $\tilde{\mathcal{E}}_D^S(k_e)$ using these different forms of the autocorrelation function $\bar{R}_D(\ell)$. We also show the turn-overs/peaks of the respective spectra k_p , $k_{e,p}$ and the corresponding factor b required to equate $k_{e,p}$ to k_p . Note, for solutions in $k_{e,p}$ with a \pm , we take the $+$ form in b as these are more in line with alternative solutions to b in Section III C. Note that for $D = 3$, the last column is equivalent to Townsend's model eddy of a swirling fluid of a characteristic size $L^{75,79}$.

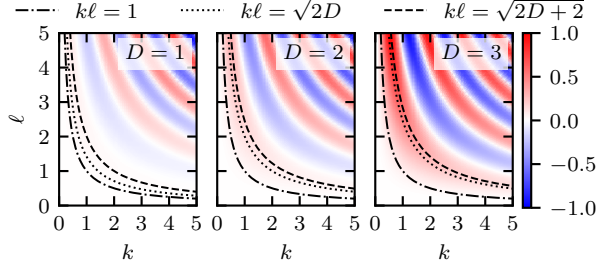


FIG. 3. Filter function $\mathcal{G}_D(k\ell)$ normalized by its maximum (in the generated grid) to $[-1, 1]$ for $D = 1, 2, 3$. The black dash-dotted, dotted, and dashed contours correspond to $k\ell = 1$, $k\ell = \sqrt{2D}$, and $k\ell = \sqrt{2D+2}$ respectively.

C. $\tilde{\mathcal{E}}_D^S(k_e)$ as a Filtered Function of $\mathcal{E}_D(k)$

An alternative method we can use to estimate a *constant* b is to describe Equation 8 as a filter on $\mathcal{E}_D(k)$

$$\tilde{\mathcal{E}}_D^S\left(\frac{b}{\ell}\right) = \int_0^\infty \mathcal{E}_D(k) \mathcal{G}_D(k\ell) dk, \quad (23)$$

where

$$\begin{aligned} \mathcal{G}_D(k\ell) &= \frac{1}{b} \ell^2 \frac{\partial}{\partial \ell} [1 - \mathcal{T}_D(k\ell)], \\ &= 2^{D/2-1} \Gamma(D/2) \frac{\ell}{b} (k\ell)^{2-D/2} \mathcal{J}_{D/2}(k\ell). \end{aligned} \quad (24)$$

which is calculated by differentiating under the integral of

$$\tilde{\mathcal{E}}_D^S\left(\frac{b}{\ell}\right) = \frac{1}{b} \ell^2 \frac{\partial}{\partial \ell} \left[\int_0^\infty [1 - \mathcal{T}(k\ell)] \mathcal{E}_D(k) dk \right], \quad (25)$$

when the spectral representation of the SF (Equation 11) is used in Equation 8.

Ideally, $\mathcal{G}_D(k\ell)$ would be a δ function-like to select from $\mathcal{E}_D(k)$ the appropriate energies for the corresponding physical scale ℓ . We now show that Equation 24 is *not* δ function-like.

To associate $k\ell$ with b we say that $k\ell = b\mathcal{K}$ where $\mathcal{K} = k/k_e$ and assert $\mathcal{K} = 1$ *i.e.*, $k_e \equiv k$. Figure 3 shows Equation 24 as a function of k and ℓ along with contours corresponding to $b = 1$, $b = \sqrt{2D}$, and $b = \sqrt{2D+2}$. We have chosen these values based on extensions of literature results^{72,75} to $D = 1, 2$, along with low-order coefficients of Taylor expansions of $\mathcal{G}_D(k\ell)$ about $k\ell = 0$. The first peak of $\mathcal{G}_D(k\ell)$ is better represented by $\sqrt{2D}$ to $\sqrt{2D+2}$. If we crudely assume that $\mathcal{G}_D(k\ell)$ behaves δ function-like, then $\mathcal{G}_D(k\ell)$ preferentially selects from $\mathcal{E}_D(k)$ at the locations corresponding to $\sqrt{2D}$ to $\sqrt{2D+2}$.

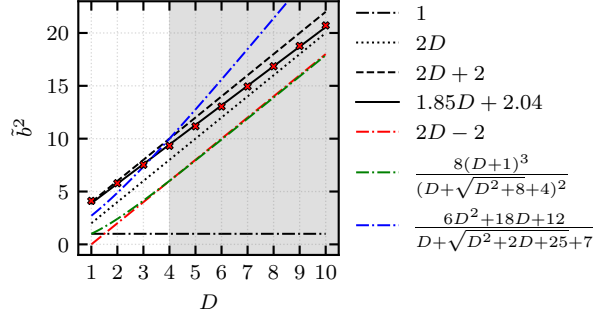


FIG. 4. The location of the first peaks ($\tilde{b} = x_{\text{peak}} = \text{argmax}\{\tilde{\mathcal{G}}_D(x)\}$) of the filter $\tilde{\mathcal{G}}_D(x) \sim x^{2-D/2} \mathcal{J}_{D/2}(x)$ as a function of dimension D . The first peak locations (red crosses) are estimated using numerical methods and the black solid line is the linear fit. The dashed and dotted black lines are some reasonable approximations. The red, green, and blue dash-dotted lines correspond to the estimates of b from Table II. Note, the estimates from Table II correspond to the *integrated* influence of $\mathcal{G}_D(k\ell)$ with $\mathcal{E}_D(k)$ rather than just one part of the integrand.

As a first-order approximation, assuming the peak of Equation 24 is where the peak of the corresponding $\tilde{\mathcal{E}}_D^S(k_e)$ is located could provide a suitable method for estimating an appropriate b for an unknown $\mathcal{E}_D(k)$. To find where these peak contours of the $\mathcal{G}_D(k\ell)$ lie, we first remove the extra ℓ dependence, and define the following 1D function

$$\tilde{\mathcal{G}}_D(x = k\ell) \equiv \mathcal{G}_D(k\ell) \frac{b}{\ell} \sim x^{2-D/2} \mathcal{J}_{D/2}(x). \quad (26)$$

We numerically evaluate $\tilde{b} = x_{\text{peak}} = \text{argmax}\{\tilde{\mathcal{G}}_D(x)\}$. As ℓ linearly scales the filter for a fixed k , $\tilde{\mathcal{G}}_D(x)$ is an appropriate substitute for $\mathcal{G}_D(k\ell)$. We show \tilde{b}^2 as a function of D in Figure 4. The linear fit $\tilde{b}^2 = 1.85D + 2.04$ is approximately our stated $\tilde{b}^2 = 2D + 2$ contour in Figure 3 for $D < 4$. Estimates from Table II are also included in Figure 4. These estimates are obtained from the peaks of Equation 23 *i.e.*, rather than from just one part of the integrand.

As $k\ell$ increases, $\mathcal{G}_D(k\ell)$ oscillates about 0 (see, Figure 3) which shows that $\mathcal{G}_D(k\ell)$ is not δ function-like. The oscillations cause $\tilde{\mathcal{E}}_D^S(k_e)$ to be influenced by $\mathcal{E}_D(k)$ across *all* scales *i.e.*, the relation has non-local influences. It also explains the dependence of \mathcal{B}, b on the form of $\mathcal{E}_D(k)$ as seen in this, and the previous sections. For a fixed ℓ , the filter peaks at $k\ell \sim \sqrt{1.85D + 2.04}$ and oscillates around 0 with increasing k . As a crude approximation, we could say $\mathcal{G}_D(k\ell)$ is δ function-like and the contributions (oscillations) at large k cancel out. However, for a PSD with large β , the difference in PSD amplitude between

adjacent wavenumbers is larger, meaning successive contributions from $\mathcal{E}_D(k)$ with $\mathcal{G}_D(k\ell)$ in Equation 23 would *not* perfectly cancel out. For $D = 1, 2$, the oscillations grow larger in amplitude with increasing k meaning the successive contributions would also not perfectly cancel out. For small β , the amplitude between adjacent wavenumbers is similar, meaning successive contributions would approximately cancel, resulting in a net zero contribution for scales $k\ell \gg 1$. The influence of the non-cancelled non-local contributions propagates into b and \mathcal{B} and explains the observation from Figure 2 that for all $D = 1, 2, 3$ at large β , the bias is large – and also explains the dependence on the form of the PSD. For $D = 1$, the bias is larger than $D = 2, 3$ because the growth in amplitude of the oscillations is greater than $D = 2, 3$.

We conclude this section by suggesting

$$b_{p,D}^{\text{est}} = \begin{cases} \sqrt{2D-2} & \text{for } D > 1 \\ 1 & \text{for } D = 1 \end{cases} = \begin{cases} 1 & \text{for } D = 1 \\ \sqrt{2} & \text{for } D = 2 \\ 2 & \text{for } D = 3 \\ \dots \end{cases}, \quad (27)$$

as a D -dependent b factor. The slope of $(b_{p,D}^{\text{est}})^2$ with D is approximately the slope of the linear fit shown in Figure 4. Equation 27 also closely represents the first two analytical solutions in Table II without the non-physical $b = 0$ for $D = 1$ from the $b = \sqrt{2D-2}$ solution. The subscript- p represents that this b is associated with correcting the *peak* (the energy-containing scale) of the equivalent spectrum. This is in contrast to the pure power law regime where the b to equate (all) the amplitudes is analytically known (b_D^{pow} , Equation 13). It is the case that $b_{p,D}^{\text{est}} \neq b_D^{\text{pow}}$. Therefore, aligning the energy-containing scales (using $b = b_{p,D}^{\text{est}}$) comes at the cost of the amplitude bias in the power law regime (see Figure 1). The accuracy of $b_{p,D}^{\text{est}}$ to align the energy-containing scales is discussed further in the next section. In Section III E, we show that the cost of using $b_{p,D}^{\text{est}}$ (instead of b_D^{pow}) in the pure power law regime can be corrected for.

D. Model Spectrum with an energy-containing Scale

Now, we define a model angle-integrated spectrum,

$$\mathcal{E}_D(k) = \Omega_D k^{D-1} \left[\left(\frac{k}{k_0} \right)^{-\alpha} e^{-k_0^2/k^2} \right], \quad (28)$$

that contains exponential growth at small k which represents a turbulence energy-containing range that has a well-defined effective energy-containing scale (peak) at $k_p = \sqrt{2k_0^2/\beta}$. The model spectrum then transitions to pure power law decay $\beta = \alpha - D + 1$ at $k \gg k_p$.

The corresponding amplitude bias function is,

$$B_D^{\text{exp}} \left(\frac{k}{k_p}, \beta, b \right) = 2^{1-\beta} b^{\beta-1} \Gamma \left(\frac{D}{2} \right) \times \mathcal{M}_{3,0}^{0,2} \left(\frac{\beta-1}{2}, 1 \frac{\alpha}{2} \left| \frac{8}{b^2 \beta} \frac{k^2}{k_p^2} \right. \right) e^{\frac{\beta}{2} \frac{k_p^2}{k^2}}, \quad (29)$$

where $\mathcal{M}_{p,q}^{m,n}$ is the Meijer G-function⁸¹. The Meijer G-function is unfortunately more analytically complicated than even the generalized hypergeometric functions! Although they can be analytically difficult to analyze, we use numerical methods that are readily available through Python packages such as `mpmath`. When Equation 28 is the Fourier spectrum, the equivalent spectrum has a systematic bias described by Equation 29. This bias is wavenumber dependent, unlike the pure power-law example from Section III A. Note that Equation 29 is applicable to *only* Equation 28 and under different $\mathcal{E}_D(k)$ (*e.g.*, different powers in the exponential term) the corresponding bias function will be different for the reasons described in Section III C.

Figure 5 shows the b required to align the position of the peaks of $\tilde{\mathcal{E}}_D^S(k_e)$ with $\mathcal{E}_D(k)$. We analytically solve for $\tilde{\mathcal{E}}_D^S(k_e)$ using Equation 23 with Equation 28⁸² then numerically find $k_{e,p}$.

We see the complexity initially discussed in Section III C: whilst the filter preferentially selects at the scale associated with $b \approx \sqrt{1.85D + 2.04}$, it is the *integration* with (the nonlinear) $\mathcal{E}_D(k)$ that determines the actual peak location of $\tilde{\mathcal{E}}_D^S(k_e)$. The factor b_p naturally depends on the form of the $\mathcal{E}_D(k)$. The previous fit of $b_p^2 = 1.85D + 2.04$ significantly differs from the analytical solutions. Given Equation 28, Figure 5 shows b depends on β and D with negligible dependence on k_0 . At (Kolmogorov) $\beta \sim 5/3$, the choice of $b_p = b_{p,D}^{\text{est}}$ (Equation 27) approximates the analytical b_p (particularly for $D = 1, 3$). We also provide a

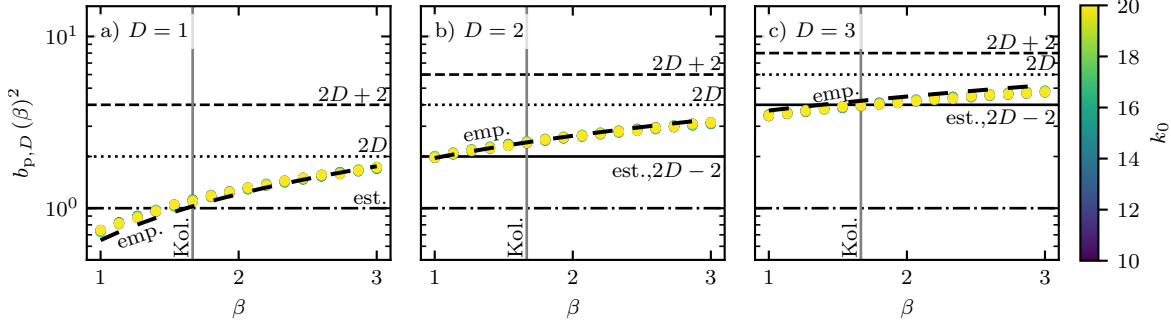


FIG. 5. b factor (b_p) corresponding to aligning the position of the peaks of $\tilde{\mathcal{E}}_D^S(k_e)$ with $\mathcal{E}_D(k)$ using the model spectrum Equation 28 for different β and k_0 values (circles). Note, the circle markers are coloured representing different k_0 (shown by the colourbar), but b_p appears almost independent of k_0 . The black horizontal lines correspond to 1 (dash-dot), $2D - 2$ (solid), $2D$ (dotted), and $2D + 2$ (dashed) as discussed in Section III C with $b_{p,D}^{\text{est}}$ denoted as “est.” where appropriate. The β -dependent thick black dashed line is the empirical formula Equation 30 ($b_{p,D}^{\text{emp}}$, denoted as “emp.”). The solid vertical gray line represents the (Kolmogorov) power law slope of $-5/3$.

β and D dependent *empirical* estimate by fitting to the data shown in Figure 5

$$b_{p,D}^{\text{emp}}(\beta) = \sqrt{\frac{\beta + D - 1}{2}} + \frac{3(D - 1) + 1}{10}. \quad (30)$$

that approximates the numerical b_p across β values. However, practically, using $b = b_{p,D}^{\text{emp}}$ would require *a priori* knowledge of β , and therefore, we largely ignore this estimate.

Figure 6 shows Equation 29 at the (equivalent) wavenumber corresponding to the effective energy-containing scale of Equation 28. We note the following:

- There is no b that allows $B_D^{\text{exp}}\left(\frac{k}{k_p} = 1, \beta, b\right) = 1$ for all $\beta \in [1, 3]$ for $D = 2, 3$. So even for a β dependent b , there will still be a systematic bias in the equivalent spectrum.
- For $D = 1$, $b_{p,D}^{\text{emp}}$ closely follows the $B_D^{\text{exp}} = 1$ contour line: the peaks of $\mathcal{E}_D(k)$ and $\tilde{\mathcal{E}}_D^S(k_e)$ are aligned in wavenumber ($k_p \approx k_{e,p}$) and amplitude: $\mathcal{E}_D(k_p) \approx \tilde{\mathcal{E}}_D^S(k_{e,p})$.
- For $D = 2$ and $D = 3$, $b_{p,D}^{\text{emp}}$ closely follows a constant contour $B_D^{\text{exp}} \approx 0.75$. The peaks are aligned in wavenumber and differ in amplitude for all β by the same constant factor: $\mathcal{E}_D(k_p) \sim \tilde{\mathcal{E}}_D^S(k_{e,p})$.

We note that at scales $k_e \ll k_p$, $\tilde{\mathcal{E}}_D^S(k_e)$ becomes negative and therefore, would not physically represent $\mathcal{E}_D(k)$ at those scales. However, in this section, we have determined

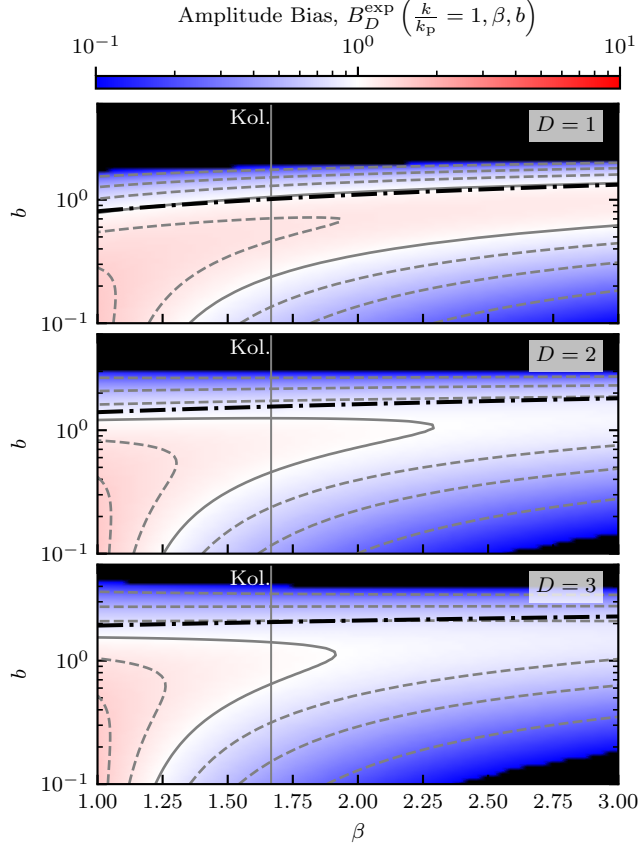


FIG. 6. Similar to Figure 1. The bias (Equation 29) at the peak of the spectrum $k = k_p$ for an angle-integrated spectrum of the form Equation 28, for Euclidean dimensions $D = 1$, $D = 2$, and $D = 3$. The line contours correspond to linear spacings of 0.25 starting from $B_D^{\text{exp}} = 0.25$ to 1.75 with $B_D^{\text{exp}} = 1$ represented by the solid gray line. The solid vertical gray line represents the (Kolmogorov) power law slope of 5/3. The dash-dotted black line corresponds to $b_{p,D}^{\text{exp}}$ (Equation 30).

appropriate b values (b_D^{emp} and $\approx b_D^{\text{est}}$) that align the effective energy-containing scales of $\tilde{\mathcal{E}}_D^S(k_e)$ to those of $\mathcal{E}_D(k)$. We will investigate the power law behaviour in the next section and show that $B_D^{\text{exp}} \rightarrow B_D^{\text{pow}}$ as $k_e \gg k_p$.

E. The Power Law Limit

Investigation of Equation 29 indicates that $B_D^{\text{exp}} \rightarrow \text{const}$ for a fixed β and b as $k \gg k_p$. We have analytically calculated the local power law index

$$\Delta\tilde{\beta}(k_e) = -\frac{d \ln(\tilde{\mathcal{E}}_D^S(k_e))}{d \ln(k_e)}, \quad (31)$$

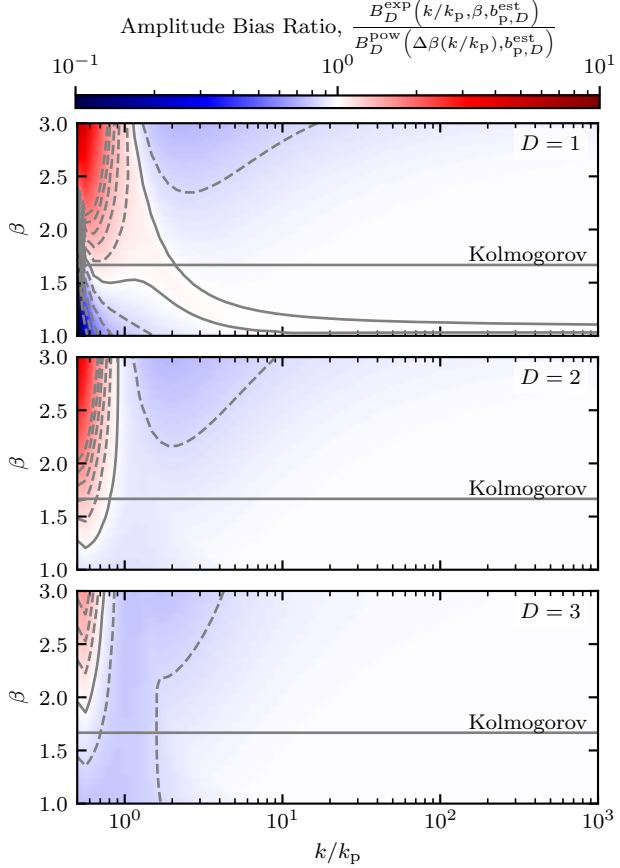


FIG. 7. The ratio of the amplitude biases Equation 29 and Equation 14 as a function of k/k_p and β , for Euclidean dimensions $D = 1$, $D = 2$, and $D = 3$. The line contours correspond to linear spacings of 0.25 starting from $B_D^{\text{exp}} = 0.25$ to 1.75 with 1 represented by the solid gray line. The solid horizontal gray line represents the (Kolmogorov) power law slope of $5/3$.

of $\tilde{\mathcal{E}}_D^S(k_e)$ corresponding to Equation 28. We note that we need to clamp $\Delta\tilde{\beta} \in (1, 3)$ as required by Equation 14. We provide $\Delta\tilde{\beta}(k_e)$ as a k_e -dependent argument to B_D^{pow} and compare $B_D^{\text{pow}}(\Delta\tilde{\beta}(k/k_p), b)$ to $B_D^{\text{exp}}(k/k_p, \beta, b)$. Figure 7 shows that we have a biased spectrum at $k \sim k_p$, and a unbiased spectrum at $k \gtrsim 10k_p$ as the ratio clearly asymptotes to 1. Therefore, we can acknowledge that $B_D^{\text{exp}} \rightarrow B_D^{\text{pow}}$ at large k . This is consistent with the findings in Section III B and Appendix A: $\tilde{\mathcal{E}}_D^S(k_e)$ will exhibit the correct pure power law behaviour (for reasonable underlying $\mathcal{E}_D(k)$) with an intrinsic amplitude bias as described by B_D^{pow} .

Previous works^{67,68} have focused on the turbulence inertial range and have made the approximation $\bar{S}_D(\ell) \propto \ell^\eta$ where $\eta = \beta - 1$ and therefore, effectively Equation 8 is of the

form⁸³

$$\tilde{\mathcal{P}}_D^S(k_e) \equiv \frac{1}{2} \frac{\eta}{b} \ell \bar{S}_D(\ell) \sim \mathcal{B} \tilde{\mathcal{E}}_D^S(k_e), \quad (32)$$

where $\tilde{\mathcal{P}}_D^S(k_e)$ is the power law region approximation to $\tilde{\mathcal{E}}_D^S(k_e)$. For an unbounded pure power law spectrum (Equation 10) then the approximation $\bar{S}_D(\ell) \sim \ell^\eta$ is exact and therefore Equation 32, Equation 12, and Equation 14 are exact. Note that the b cases discussed in Section III A are still present – either b is β dependent, or b is constant with the specific value being ambiguous (see previous sections) and $\tilde{\mathcal{P}}_D^S(k_e)$ has a systematic amplitude bias described by Equation 14.

Using the model spectrum of Equation 28 with the equivalent spectrum power law approximation (Equation 32), we get the following amplitude bias function

$$\begin{aligned} \tilde{B}_D^{\text{exp-pow}} \left(\frac{k}{k_p}, \beta, b \right) = & \frac{F}{b} e^{\frac{\beta}{2} \frac{k_p^2}{k^2}} \left(\frac{k_p}{k} \right) \left[\right. \\ & 2^{3\beta/2} D b \sqrt{\beta} \left(\frac{k}{k_p} \right)^\beta \Gamma \left(\frac{\beta-1}{2} \right) \\ & \left. -4\sqrt{2} b^\beta \beta^{\beta/2} \frac{k}{k_p} \mathcal{M}_{3,0}^{0,2} \left(\frac{\beta+1}{2}, 1 \frac{\alpha}{2} \left| \frac{8}{b^2 \beta} \frac{k^2}{k_p^2} \right. \right) \Gamma \left(\frac{D}{2} + 1 \right) \right] \end{aligned} \quad (33)$$

where $F = 2^{-\beta-3/2} \beta^{-\beta/2} (\beta-1) / D$. This bias function is shown in Figure 8 for $b = 1$. In the pure power law region $k \gg k_p$, the bias asymptotes to a constant for a fixed β . As with B_D^{exp} (Equation 29), $\tilde{B}_D^{\text{exp-pow}}$ approaches B_D^{pow} for $k \gg k_p$.

Previous applications of $\tilde{\mathcal{E}}_D^S(k_e)$ in the literature have used the pure power law approximation form $\tilde{\mathcal{P}}_D^S(k_e)$ (Equation 32)⁶⁷⁻⁶⁹. Similar to Figure 1 and Figure 10, Figure 8 explains its success. For any reasonable underlying spectrum $\mathcal{E}_D(k)$, the turbulence inertial range is well captured by $\tilde{\mathcal{E}}_D^S(k_e)$ (and $\tilde{\mathcal{P}}_D^S(k_e)$) with an amplitude bias that is described by $B_D^{\text{pow}}(\beta, b)$.

We have shown that we can debias (apply a systematic correction to) the equivalent spectrum in the pure power law regime, assuming that we can estimate the correct power law. We have also shown that the equivalent spectrum will exhibit the correct power law behaviour at large k (for $1 < \beta < 3$)^{20,22,57}. This will form the basis for a model independent debiasing technique which is introduced and discussed in the next section.

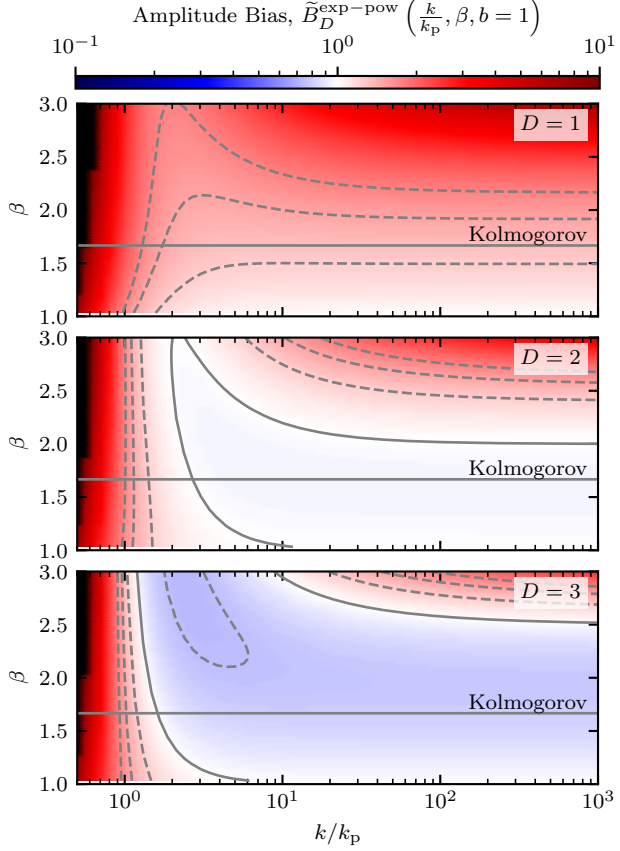


FIG. 8. The amplitude bias (Equation 33) of the power law approximation for the model spectrum Equation 28 as a function of k/k_p and β with $b = 1$, for Euclidean dimensions $D = 1$, $D = 2$, and $D = 3$. The line contours correspond to linear spacings of 0.25 starting from $\tilde{B}_D^{\text{exp-pow}} = 0.25$ to $\tilde{B}_D^{\text{exp-pow}} = 1.75$ with 1 represented by the solid gray line. The solid horizontal gray line represents the (Kolmogorov) power law slope of $5/3$.

F. Summary

In summary of this section, we have found that the equivalent spectrum has a systematic bias in amplitude for different Fourier spectra. In the pure power-law case, this bias is readily determined and depends on β , D , and b . We have examined two cases. Firstly, if we assume b is β -dependent, then this systematic bias can be cancelled out. However, this method would be difficult to implement on real observations. In addition, the Fourier spectrum is of a different form *e.g.*, contains an exponential growth region, then a β -dependent b cannot exactly equate the equivalent spectrum to the Fourier spectrum at the peaks of the spectra – there will still be a systematic bias in the equivalent spectrum. Secondly, we could assume b

is constant and obtain a physically motivated relationship between wavenumber and physical lag-scale $k_e = b/\ell$. Although there is ambiguity in values for b (that are dependent on the form of the Fourier spectrum), we provide constant b values that are appropriate to align the peaks of the equivalent spectrum to the Fourier spectrum. We can then apply a general-purpose debiasing technique to reduce the systematic bias present in the equivalent spectrum to obtain a better estimate of the Fourier spectrum. This method is far more practical for implementation on real observations.

IV. IMPLEMENTATION AND VALIDATION

In Section III (particularly, Section III E), we have built the intuition that the behaviour of $\tilde{\mathcal{E}}_D^S(k_e)$ is consistent with $\mathcal{E}_D(k)$ for regions where $\mathcal{E}_D(k)$ is a power law. We will start this section by introducing the practical implementation of $\tilde{\mathcal{E}}_D^S(k_e)$ and the method for debiasing based on Section III E. This will do away with the need for the bias functions which requires modelling the underlying spectrum. We then validate the implemented method on fBm fields and compare the results to analytical expressions from Section III.

A. Implementation

To calculate our estimate $\tilde{\mathcal{E}}_D^S(k_e)$, via the second-order structure function $\bar{S}_D(\ell)$, we perform the following steps in order, with bullet points indicating recommendations and additional details:

Step 1: Calculate the averaged second-order structure function $\bar{S}_D(\ell)$.

- Calculating $\bar{S}_D(\ell)$ can be done using codes like `fastSF`¹⁸ or our provided Python code on Github.
- Usually, $\bar{S}_D(\ell)$ has low amplitude-high frequency oscillations which can propagate into the derivative(s) when calculating $\tilde{\mathcal{E}}_D^S(k_e)$ which results in a noisy spectral estimate^{84,85}. Therefore, we suggest binning, or smoothing $\bar{S}_D(\ell)$ before moving onto the next step. We urge readers to exercise caution when binning the SF. Over-binning can lead to the loss of information that reflects the true turbulence statistics – associated with intermittency effects, for example – and could bias

scaling exponent estimates^{86,87}. Future work will need to examine the influence of different binning procedures and binning scales.

In this paper, we bin $\bar{S}_D(\ell)$ in log-space *i.e.*, the bins are equally spaced in log-space. Due to our binning implementation, depending on the number of bins and the span of the data, some bins incorporate no data. In those cases, we interpolate those missing values (in log-space) based on the surrounding bins. We typically use between 16 and 64 bins. This is chosen based on visually comparing the binned to un-binned $\bar{S}_D(\ell)$ – we wish to retain as many features as possible whilst removing any high-frequency oscillations (which are particularly present at large ℓ).

- Practically, at large ℓ , $\bar{S}_D(\ell)$ tends to have large fluctuations around the value of twice the variance (Equation 4) as it samples inhomogeneities beyond the correlation scale⁸⁸. We recommend stopping at a maximum lag $\ell_{\max} \lesssim \frac{N}{2}\Delta x$ where $\Delta x = \mathcal{L}/N$ is the discretized sampling spacing.

Step 2: Create the “Uncorrected” estimate $\tilde{\mathcal{E}}_D^S(k_e)$ by using Equation 8 with an appropriate b .

- We use `numpy.gradient` which uses a second-order central differences method with first-order forwards/backwards differences at the boundaries.
- Appropriate b are: b_D^{est} (Equation 27), and b_D^{emp} (Equation 30). To use b_D^{emp} will require either *a priori* spectral slope knowledge, or a second correction will need to be applied after an initial guess of b which can be used to understand the appropriate β and therefore b_D^{emp} . We use b_D^{est} .
- $\tilde{\mathcal{E}}_D^S(k_e)$ creates an estimate for $\mathcal{E}_D(k)$ that still requires the systematic correction to the amplitude (as shown in the analysis in Section III). The “Uncorrected” estimate will form an initial guess and its properties can be used to better understand the correction required.
- We interpolate the k_e of $\tilde{\mathcal{E}}_D^S(k_e)$ onto the same k as $\mathcal{E}_D(k)$. The discrete wavenumber spacing is $m\Delta k$ where $\Delta k = 2\pi/\mathcal{L}$ and the discrete lag spacing is $\ell = n\Delta x$ for integers $n, m \in [1, N/2]$. The equivalent wavenumber $k_e = z\Delta k_e$ will therefore have non-integer spacing according to $z = n^{-1}$ where $\Delta k_e = bN/\mathcal{L}$. Given

$k \in [2\pi/\mathcal{L}, \pi N/\mathcal{L}]$ for $m \in [1, N/2]$ and $k_e \in [2b/\mathcal{L}, bN/\mathcal{L}]$ for $z^{-1} = n \in [1, N/2]$, it would be natural to conclude $b = \pi$. However, Section III suggests otherwise. As a result, we cut $\tilde{\mathcal{E}}_D^S(k_e)$ so that $\max\{k_e\} = \min\{\pi N/\mathcal{L}, bN/\mathcal{L}\}$ and $\min\{k_e\} = \max\{2\pi/\mathcal{L}, 2b/\mathcal{L}\}$.

Step 3: Estimate the local power law slope of the “Uncorrected” estimate $\Delta\tilde{\beta}(k_e) = -\frac{d \ln(\tilde{\mathcal{E}}_D^S(k_e))}{d \ln(k_e)}$.

- Once again, we use `numpy.gradient`.
- We emphasize that this does *not* require a-priori knowledge of the spectral index
 - a local power law index is estimated numerically, at every k -value on the grid.
- $\Delta\tilde{\beta}(k_e)$ is (roughly proportional to) the second derivative of $\bar{S}_D(\ell)$ which emphasizes the need to bin and/or smooth $\bar{S}_D(\ell)$, $\tilde{\mathcal{E}}_D^S(k_e)$, and $\Delta\tilde{\beta}(k_e)$. Noise from the first derivative ($\tilde{\mathcal{E}}_D^S(k_e)$) propagates into the second derivative ($\Delta\tilde{\beta}$)⁸⁹.
- Since $B_D^{\text{pow}}(\beta, b)$ is only valid for $1 < \beta < 3$ (Section III A), we clamp to $1.01 < \Delta\tilde{\beta}(k_e) < 2.99$.
- We apply a final step of binning and interpolation. We bin in log-space to between 4 and 16 data-points. We find that this is often enough to describe the local power law for power law spectra. Interpolate back onto k_e for easy use in the next step.

Step 4: Finally, take the “Uncorrected” spectrum and estimate the “Debiased” form of the equivalent spectrum: $\mathcal{B}^{-1}\tilde{\mathcal{E}}_D^S(k_e)$ where $\mathcal{B} = B_D^{\text{pow}}(\Delta\tilde{\beta}(k_e), b)$.

- Figure 7 is equivalent to the error obtained by using this local de-biasing technique for a Fourier spectrum of the form Equation 28. This is suitable as a general approach method where the underlying spectrum is largely unknown, or the analytical formula for the bias is difficult to obtain. Additionally, the Γ -functions in Equation 14 are more easily tractable from Python packages like `scipy` compared to $\mathcal{M}_{3,0}^{0,2}$.

We provide these steps as Python code on Github.

B. fBm Validation

We now consider fractional Brownian motion fields (fBm) with spectral shape specified in Equation 28. Our fBm fields are used solely for testing purposes as we know exactly what power law we expect and they are quick to generate. We generate the field $s_D(\mathbf{x})$ using a spectral synthesis method⁹⁰ by defining:

$$\hat{s}_D(\mathbf{k}) = \sqrt{\frac{E_D(\mathbf{k})}{E^{\text{total}}}} (\cos(\boldsymbol{\theta}) + i \sin(\boldsymbol{\theta})), \quad (34a)$$

$$E_D(\mathbf{k}) = \begin{cases} 0, & |\mathbf{k}| < k_{\min} \\ 0, & |\mathbf{k}| > k_{\max}, \\ \left(\frac{|\mathbf{k}|}{k_0}\right)^{-\alpha} e^{-k_0^2/|\mathbf{k}|^2}, & \text{otherwise} \end{cases} \quad (34b)$$

where $E^{\text{total}} = \int_{-\infty}^{\infty} E_D(\mathbf{k}) d^D \mathbf{k}$ is the total energy, (*i.e.*, we have normalized so that the energy of the fBm field is 1), and $\boldsymbol{\theta}$ are the random phases sampled from a uniform distribution from 0 to 2π . Practically, when the number of grid points N is uniformly sampled in the physical domain \mathcal{L} : k_{\min} corresponds to the discrete wavenumber spacing $\Delta k = 2\pi/\mathcal{L}$ and k_{\max} corresponds to the Nyquist wavelength $\pi N/\mathcal{L}$. We then take the inverse Fourier transform of $\hat{s}_D(\mathbf{k})$ to obtain the fBm field $s_D(\mathbf{x})$.

Fractional Brownian motion fields have been used extensively to validate methods for interstellar turbulence^{30,91–95}, with modifications using Perlin noise as the basis functions or exponentiating^{96,97}. They have similarly been used for the ICM, when measuring the turbulence structure from rotation measure observations⁹⁸ and ICM telescope & method testing⁹⁹. It is important to note that these fields are *not* turbulent since they are missing higher-order features like intermittency. The equivalent spectrum derivation makes the assumption of homogeneity (at Equation 3) which could have significant consequence. However, this could also have small consequence as we are looking at second-order statistics only (autocorrelation, power spectrum, structure function) which are minimally influenced by the higher-order effects of intermittency and non-Gaussianity. The influence of intermittency on $\tilde{\mathcal{E}}_D^S(k_e)$ will be left for future work. Though, we do apply the technique to observations of the turbulent solar wind in Section V.

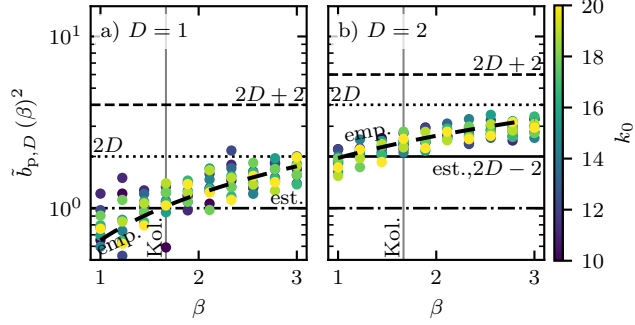


FIG. 9. Similar to Figure 5. The b factor (b_p) corresponding to aligning the position of the peaks of $\tilde{\mathcal{E}}_D^S(k_e)$ and $\mathcal{E}_D(k)$ using fBm fields with a spectrum of Equation 28 for different β and k_0 values (circles, with the colour bar representing different k_0). The black horizontal lines correspond to 1 (dash-dot), $2D - 2$ (solid), $2D$ (dotted), and $2D + 2$ (dashed) as discussed in Section III C with $b_{p,D}^{\text{est}}$ denoted as “est.” where appropriate. The β -dependent thick black dashed line is the empirical formula Equation 30 ($b_{p,D}^{\text{emp}}$, denoted as “emp.”). The solid vertical gray line represents the (Kolmogorov) power law slope of $-5/3$.

1. Bias Validation

We generate $D = 1$ and $D = 2$ fBm fields, sampling a range of $\alpha \in [D, D + 2]$ corresponding to $\mathcal{E}_D(k)$ power law $\beta \equiv \alpha - D + 1 \in [1, 3]$ and $k_0 \in [10, 20]$. For $D = 1$ we set $N = 10^6$ and for $D = 2$ we set $N = 2048$ with $\mathcal{L} = 2\pi$.

Performing a similar technique that was used to produce Figure 5, we calculate $\mathcal{E}_D(k)$ and $\tilde{\mathcal{E}}_D^S(k_e)$ for each fBm field and estimate the effective energy-containing scales k_p and $k_{e,p}$. Figure 9 shows the estimate for b_p : the b -factor required to equate $k_{e,p}$ to k_p . We see that the fBm fields follow $b_{p,D}^{\text{emp}}$. There is some noticeable scatter, likely due to the numerical differentiation and the binning and interpolation procedure.

Figure 10 ($D = 1$) and Figure 11 ($D = 2$) compare the amplitudes of $\tilde{\mathcal{E}}_D^S(k_e)$ to $\mathcal{E}_D(k)$ of the fBm fields at the effective energy-containing scale (of $\mathcal{E}_D(k)$: $k, k_e = k_p$) and in the asymptotic pure power law range ($k, k_e \gg k_p$). Values for the power law range are determined by selecting a single k where $k, k_e \gg k_p$. The structure function is sampled with linear spacing Δx . The linear spacing of Δx corresponds to k_e with non-linear, non-integer spacing (proportional to $z = 1/n$ for $n \in [1, N/2]$) which leads to few data points in log-spaced bins at large k_e . This can result in poor numerical derivative estimates at the large k_e .

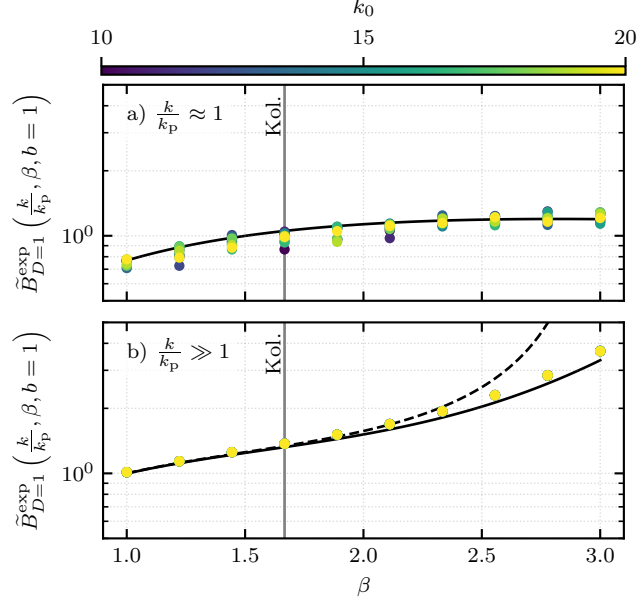


FIG. 10. The ratio of the amplitude of $\tilde{\mathcal{E}}_D^S(k_e)$ to $\mathcal{E}_D(k)$ of $D = 1$ fBm fields of different β and k_0 at (a) the peak $k, k_e \approx k_p$ and in (b) the power law regime $k, k_e \sim 30k_p$. The black solid line corresponds to the analytical B_D^{\exp} (Section III D). The black dashed line corresponds to the analytical B_D^{pow} (Section III A). The solid vertical gray line represents the (Kolmogorov) power law slope of $-5/3$.

By increasing the resolution (decreasing Δx) larger k_e can be determined more accurately. Due to these resolution effects, numerical noise dominates at large k_e so we are limited to $k, k_e = 30k_p$ for Figure 10 and $k, k_e = 5k_p$ for Figure 11. At larger k_e than selected, without the numerical noise, we expect B_D^{\exp} will approach B_D^{pow} (Section III E). The fBm amplitude biases for both Figure 10 and Figure 11 match the analytical expression well with only a small amount of scatter in Figure 10(a).

Since the fBm fields match so well to the analytical expressions, we have confidence in an appropriate selection for b and \mathcal{B} to correct for the systematic biases in $\tilde{\mathcal{E}}_D^S(k_e)$. An initial estimate $\tilde{\mathcal{E}}_D^S(k_e)$ can be corrected for by choosing an analytical expression for \mathcal{B} . There is a bit of leeway in a suitable choice of b as there is some scatter in Figure 9. Either $b = b_{p,D}^{\text{est}}$, or $b = b_{p,D}^{\text{emp}}$ would be natural choices. We recommend $b = b_{p,D}^{\text{est}}$ due to the simplicity. The factor $b_{p,D}^{\text{emp}}$ requires prerequisite knowledge of β or an additional correction step. At the Kolmogorov slope $\beta \sim 5/3$, $b_{p,D}^{\text{est}}$ is an appropriate estimate to $b_{p,D}^{\text{emp}}$.

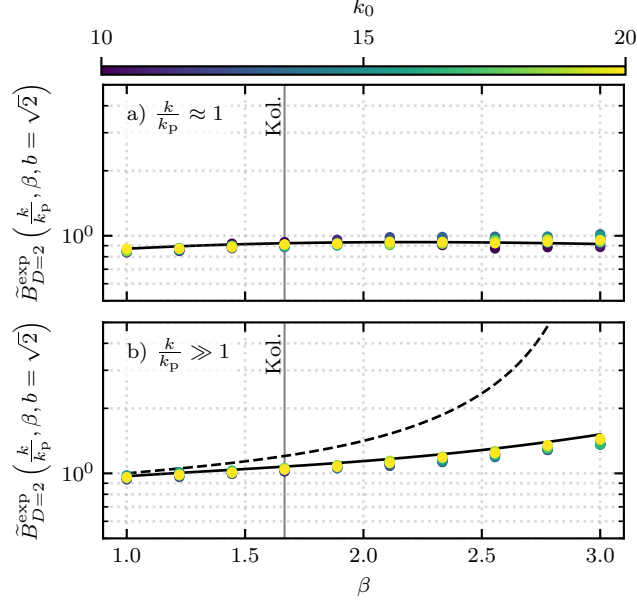


FIG. 11. Similar to Figure 10 for $D = 2$. In panel (b) $k, k_e \sim 5k_p$.

2. Large 1D fBm Validation

As additional validation, we have created a large ($N = 10^7$) 1-dimensional fBm field using the spectral synthesis method (with $\mathcal{L} = 2\pi$, $k_0 = 20$, $\beta = 5/3$). We compare the bias (ratio) of $\tilde{\mathcal{E}}_D^S(k_e)$ to $\mathcal{E}_D(k)$. The “ground truth”, $\mathcal{E}_D(k)$, is a typical Fourier transform PSD (the Periodogram²) calculated via the FFT. We test with two debiasing functions: B_D^{pow} and B_D^{exp} .

Figure 12 shows that the “Uncorrected” curve $\tilde{\mathcal{E}}_D^S(k_e)$ is noisy at $k_e \sim k_p$ and at $k_e \gtrsim 10^3$. This highlights the necessity of smoothing as the noise will propagate into $\Delta\tilde{\beta}$ and then into $\mathcal{B}^{-1}\tilde{\mathcal{E}}_D^S(k_e)$. The binning we have applied is by-eye examined to ensure the important features (slopes and scales) are retained – future work will focus on the case of intermittent signals as well as for signals with data gaps. The “Uncorrected (binned)” curve correctly reduces the noise at $k_e \sim k_p$. Our simple smoothing and binning steps are unable to significantly reduce the noise at $k \gtrsim 10^4$. The “Uncorrected” and “Uncorrected (binned)” spectrum follows $B_D^{\text{pow}}(b = 1, \beta = 5/3)$ at $1 \lesssim k/k_p \lesssim 10^4$ as asserted by our analytical analysis in Section III E.

The two “Debiased” $\mathcal{B}^{-1}\tilde{\mathcal{E}}_D^S(k_e)$ are functionally identical to $\mathcal{E}_D(k)$ when $30 \lesssim k/k_p \lesssim 2 \times 10^3$. For all versions of $\tilde{\mathcal{E}}_D^S(k_e)$ (“Uncorrected”, “Uncor. (binned)”, “Debiased, B_D^{pow} ”, “Debiased, B_D^{exp} ”), the bias at k_p is small. As $k_e \rightarrow 0$ (which corresponds to $\ell \rightarrow \infty$)

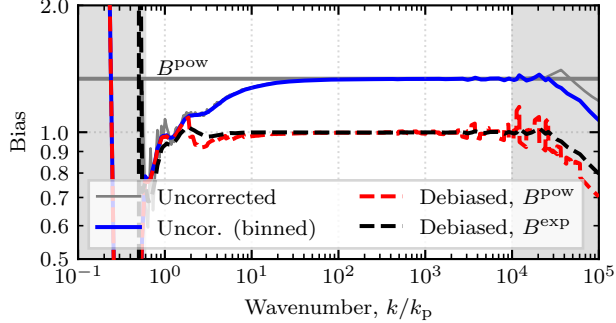


FIG. 12. Bias ($\tilde{\mathcal{E}}_D^S(k_e)/\mathcal{E}_D(k)$) of the equivalent spectrum $\tilde{\mathcal{E}}_D^S(k_e)$ compared to the “ground truth” FFT-based estimate for $\mathcal{E}_D(k)$. The gray curve is the initial $\tilde{\mathcal{E}}_D^S(k_e)$ and the blue line shows the same $\tilde{\mathcal{E}}_D^S(k_e)$ but we have binned and interpolated to reduce the high-frequency noise. The gray horizontal line shows the constant pure power law bias $B_D^{\text{pow}}(b = 1, \beta = 5/3)$. The red dashed line shows de-biasing using $\mathcal{B} = B_D^{\text{pow}}(\Delta\tilde{\beta}, b = 1)$. The black dashed line corresponds to debiasing using $\mathcal{B} = B_D^{\text{exp}}(k/k_p, b = 1, \beta = 5/3)$. The gray shaded regions indicate (roughly) where the errors become large.

$\bar{S}_D(\ell) \rightarrow \text{const.}$ which means $d\bar{S}_D(\ell)/d\ell \rightarrow 0$. We expect the $k_e \lesssim k_p$ region will not necessarily capture the exponential growth that we have modelled. At $k/k_p \gtrsim 10^3$, the “Debiased, B_D^{pow} ” curve has large fluctuations around the expected value. This is due to the numerical noise for $\Delta\tilde{\beta}$ propagating into B_D^{pow} .

The results for “Debiased, B_D^{pow} ” appear equivalent to “Debiased, B_D^{exp} ”, but “Debiased, B_D^{exp} ” theoretically only applies to the spectral model of the form Equation 28. For simplicity and robustness, in Section V, we will stick to debiasing using B_D^{pow} with a local power law estimate $\Delta\tilde{\beta}$. The disadvantage of using $\Delta\tilde{\beta}$ is that it is equivalent to using a second derivative of $\bar{S}_D(\ell)$ which results in the numerical difficulties at large k_e .

V. EXAMPLES

We apply $\tilde{\mathcal{E}}_D^S(k_e)$ to simulated and genuine data products with suitable resolution and for dataset dimensions $D = 1, 2, 3$. For comparison, we generate a “ground-truth” $\mathcal{E}_D(k)$ using a typical Fourier transform method (*i.e.*, Periodogram) via the FFT^{2,5}.

We now emphasize some additional important caveats. The spectra, $\tilde{\mathcal{E}}_D^S(k_e)$ and $\mathcal{E}_D(k)$, correspond to the spectra representing the *dataset*. Usually, the dimension of the

dataset D is *not* equal to the dimension of the system. In other words, observations typically obtain projections and slices of the full (usually 3D) system – we have lost information. Nonetheless, the spectra, $\tilde{\mathcal{E}}_D^S(k_e)$ and $\mathcal{E}_D(k)$, are associated with the *dataset* and their associated biases, b and \mathcal{B} , are assumed to be the same as investigated above with D given by the dataset dimension.

The relations of the spectra of the dataset to the spectra of the system can be non-trivial. Additionally, aliasing issues can be introduced resulting from mis-interpreting Fourier modes in the observation that are associated with the un-observed dimensions. These issues are present in *all* situations where the full system cannot be observed. We describe some of these cases for the examples that we show in this section in more detail in Appendix B 2.

Note that the analyses in this section are not intended to be a breakdown or discussion on PSD themselves, or provide any physical insights. We merely compare the equivalent spectrum to traditionally accepted techniques on high-fidelity data across a range of data-types.

A. Solar Wind, $D = 1$

Viewed as a natural wind tunnel, the solar wind as a “laboratory” for plasma turbulence experiments^{37,39,42} is unique as it provides decades of high-resolution in-situ astrophysical plasma turbulence observations. As a result, the solar wind spectrum is remarkably well studied¹⁰⁰. The solar wind has also been used in previous analyses of the equivalent spectrum^{67,68}.

Solar wind obervations are performed by sensors that generate a time-series of data. In other words, the observations have a dataset dimension of $D = 1$ (all time-series observations have dataset dimension $D = 1$). Of course, the solar wind magnetic field fluctuations are determined by a system that is spatially *not* 1D *i.e.*, the system dimension > 1 . Given some additional assumptions (such as Taylor’s hypothesis), the time-series observations can be assumed to approximate a 1-dimensional spatial slice of the physical system. We discuss additional intricacies with estimating spectra associated with $D = 1$ observed slices in Appendix B 2.

Some solar wind observations rely on multiple spacecraft such as the Magnetospheric Multiscale (MMS) mission¹⁰¹. The unique measurement capabilities of MMS, which are a

set of satellite that fly in formation, enables direct access to measurements with a handful of fixed spatial separations. These spatial separations probe specific equivalent wavenumbers of the spectrum using the same data (which would not be possible to estimate using traditional Fourier techniques). This application is an advantage of the *equivalent spectrum*⁶⁷.

We use data from *Wind*¹⁰² which has been at Lagrange point 1 (≈ 1 au) since May 2004. One month [2007/01/01–2007/02/01] of calibrated version 4 (datatype “h4-rtn”) solar wind magnetic field data from the *Wind* magnetic field instrument (MFI) is obtained using PySPEDAS. The data are $D = 1$ time series observation that has $N = 28,955,151$ data points for each magnetic field component $\mathbf{b}(t) = (b_R(t), b_T(t), b_N(t))$ in units of nT, with a sampling spacing of $\Delta t \approx 0.092$ s. We obtain the fluctuations by $\delta\mathbf{b}(t) = \mathbf{b}(t) - \langle \mathbf{b}(t) \rangle$ where $\langle \cdot \rangle$ is the temporal average over the entire interval. We apply a 1% Tukey window to each $\delta\mathbf{b}(t)$ to reduce aliasing effects³⁶. The structure function, its corresponding PSD estimates and the Periodogram estimates are calculated on this windowed data.

The solar wind data (shown un-windowed in Figure 13(a)) has Fourier PSD estimates according to solar wind turbulence phenomenology at 1 au which are shown in Figure 13(b,c,d) with the following distinct regions of interest:

- At the largest scales (smallest frequency, ω) the solar wind PSD measures the temporal variability of the source of the solar wind (the Sun) and exhibits a ω^{-1} power law^{103,104}. This is often called the $1/f$ or pink noise range. In this region, since $\beta \approx 1$, B_D^{pow} is minimal (see Section III A). Therefore, the “Uncorrected” and “Debiased” estimates are similar, if not identical. See Figure 13(c) for an inset/close-up. The “Uncorrected” and “Debiased” estimates closely follow the “Binned” $\mathcal{E}_D(k)$ because B_D^{pow} is ≈ 1 .

The correlation length, λ_C , is an outer/energy-containing scale²² that represents the largest typical scale over which the turbulent fluctuations are correlated. The correlation length λ_C varies $\sim \lambda_C^{-1/2}$ as the radial distance increases from the sun¹⁰⁵ and also over sample and time¹⁰⁶, but typically, is of the order $\sim 10^6$ km at 1 au^{107,108}. The spectrum follows ω^{-1} scaling for $\omega < U/\lambda_C \sim 0.0004$ Hz.

At scales $\omega \gtrsim U/\lambda_C$, the $1/f$ range transitions to a turbulence inertial range.

- The turbulence inertial range is where the classic MHD turbulence phenomenology is observed with a $\omega^{-5/3}$ power law corresponding to the Kolmogorov turbulence phenomenology²⁴. The solar wind is a highly dynamic environment so depending on

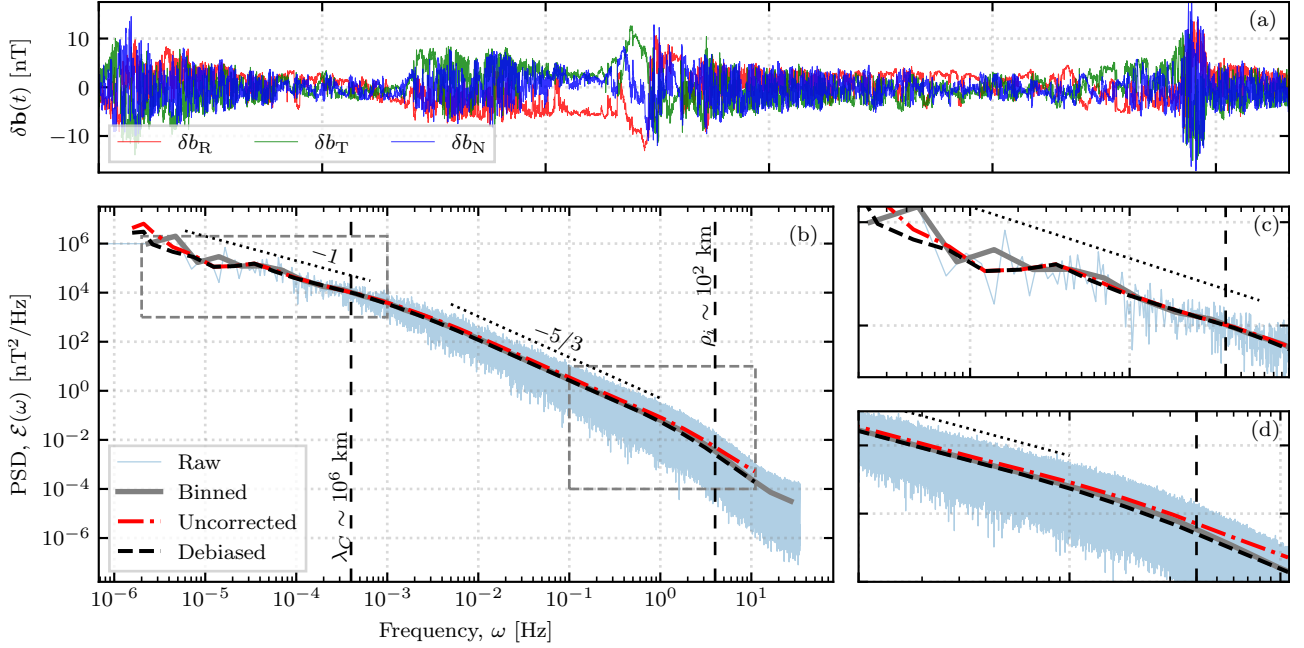


FIG. 13. (a) 1 month of *Wind* solar wind magnetic field component fluctuation data. (b) PSD estimate (Periodogram) of the data in (a) raw (solid blue), and binned (solid gray). The dash-dot red line indicates the equivalent spectrum $\tilde{\mathcal{E}}_D^S(k_e)$ with $b = 1$. The black dashed line shows $\tilde{\mathcal{E}}_D^S(k_e)$, we have debiased the initial estimate of $\tilde{\mathcal{E}}_D^S(k_e)$ by using $\mathcal{B} = B_D^{\text{pow}}$ and $\Delta\tilde{\beta}$. The black dashed vertical lines show the approximate scales where the spectrum is expected to change slope: the correlation scale λ_C , and the ion gyro-radius ρ_i . (c), (d) show zoomed-in insets from (b) as indicated by the gray dotted boxes near to λ_C and ρ_i respectively.

the realization associated with the observation dataset, departures from Kolmogorov $\beta = 5/3$ can be observed^{41,109–111}. The spectrum begins to steepen past $\omega \gtrsim U/\lambda_C$ and transitions to a $\beta \sim 5/3$ cascade region. When the spectrum is steeper there is a small bias in amplitude of the “Uncorrected” estimate. Yet, the behaviour of the “Uncorrected” curve remains consistent with $\mathcal{E}_D(k)$ *i.e.*, the correct power law is obtained.

At first glance, it may appear that the “Uncorrected” power law slope is shallower than $5/3$. As discussed in Section III D and Section III E, $\tilde{\mathcal{E}}_D^S(k_e)$ will have the correct power law at $\omega \gtrsim 10\omega_p$ where ω_p is the effective energy-containing scale (in this case, $\sim U/\lambda_C$). In the inertial range, at large ω , $\Delta\tilde{\beta} \sim 5/3$.

The “Debiased” spectrum almost exactly follows the “Binned” $\mathcal{E}_D(k)$. The bias in the

“Uncorrected” curve is well described by B_D^{pow} using $\Delta\tilde{\beta}$.

The inertial range is bounded at the largest scale by λ_C and the smallest scale by dissipation effects. In the nearly-collisionless solar wind, a relevant dissipation scale is the ion-gyro scale ρ_i .

- In the solar wind, the kinetic effects modify the cascade at scales comparable to the ion kinetic scale. When the plasma beta ≥ 1 this scale is the ion-gyroradius. At 1 au, at the scales where the ions (protons) gyrate around the magnetic field are $\rho_i \sim 10^2 \text{ km}^{112-114}$, the MHD fluid description fails and kinetic effects begin to dominate. From Taylor’s hypothesis $U/\rho_i \sim 4 \text{ Hz}$. The dynamics in this region are debated and depend on a wide range of conditions, but overall, a steepening of the spectrum (from 5/3) is expected^{100,115}.

Figure 13(b,d) shows that the spectrum departs from $\beta \sim 5/3$ as $\omega \gtrsim U/\rho_i$. The amplitude bias in the “Uncorrected” curve becomes larger. Once again, this effect is due to the intrinsic bias in the amplitudes of the spectral estimate for power law behaviour that is corrected for when debiased. The “Debiased” estimate yields a similar result to the binned periodogram estimate.

At larger β , and at the transition region around $\omega \sim U/\rho_i$, using B_D^{pow} with $\Delta\tilde{\beta}$ still adequately describes the bias in the “Uncorrected” curve.

For the regions where the bias is ≈ 1 (*i.e.*, where the spectrum is $\sim \omega^{-1}$), the “Uncorrected” estimate well represents the $\mathcal{E}_D(k)$. Since the behaviour of the spectrum is almost entirely power law, the choice of b is not significant for the outcome of the “Debiased” curve but for a consistent argument we have chosen $b = 1$ (b_D^{est}) and applied the appropriate debiasing function B_D^{pow} . Overall, the “Uncorrected” curve yields similar behaviour to $\mathcal{E}_D(k)$ with a small amplitude error in the ω^{-1} and $\omega^{-5/3}$ power law regimes respectively. The “Debiased” $\mathcal{B}^{-1}\tilde{\mathcal{E}}_D^S(k_e)$ closely follows $\mathcal{E}_D(k)$ at all scales with minimal error. Our spectral estimates are consistent with literature and expected solar wind turbulence phenomenology¹⁰⁰.

B. Interstellar Medium, $D = 2$

Telescope observations using wavelengths from radio-waves to gamma-rays often provide 2-dimensional images of gas, dust, and plasma. Spectral analyses on these images have been

used to understand the dynamics of *e.g.*, the Milky Way’s interstellar medium (ISM)^{50,51,116}, the ISM of other galaxies^{52,53,117}, the intracluster medium of galaxy clusters^{54–56,78}, and the cosmic microwave background^{118,119}.

The Local Group is a prime candidate for understanding processes in galaxies¹²⁰, enabling exceptionally high-fidelity data from our neighbourhood (astronomically speaking). Within our Local Group, the Large Magellanic Cloud (LMC) is an irregular dwarf galaxy with a single spiral arm¹²¹ that spans an angular diameter distance of $\approx 10.7^\circ$ in the sky¹²². We use already processed available data which makes use of a spectral feathering technique combining data from a range of telescopes to provide a higher-resolution observation and therefore spectral range^{123,124}. We use the Herschel Photodetector Array Camera and Spectrometer (PACS)¹²⁵ 160 μm band¹²⁴. Observations of far-infrared radiation corresponds to thermal emission from dust heated by starlight¹²⁶ and can be used to constrain dust properties such as surface density and temperature^{127,128}.

Data with sharp boundaries can introduce aliasing artefacts into the Fourier transform¹²⁹. Astronomical literature typically reduces these artefacts via window functions^{36,130,131} or by estimating the PSD by the Δ -variance^{57–59} or difference-of-Gaussian^{55,60,132} techniques. We take a central 9000^2 section of the provided foreground subtracted data and apply a 25% Tukey window to reduce sharp boundaries. Seen in Figure 14(b), the image is effectively padded with 0’s and smoothed at the edges of the LMC.

Figure 14(a) shows the PSD estimates for the data $s_2^{\text{obs}}(\mathbf{x})$ (with dataset dimension $D = 2$ and $\mathbf{x} \in \mathbb{R}^2$) in (b). Literature spectral analysis of the LMC over a range of wavelengths and telescopes provides a consistent power law of $\beta \sim 1$ ¹³³. This is compatible with our analysis. ISM analyses typically use the angle-*averaged* spectrum which is obtained by averaging over a spherical shell $\mathcal{S}(k)$ of radius $k = |\mathbf{k}|$,

$$\bar{E}_2(k) = \frac{1}{2\pi k} \int E_D(\mathbf{k}) d\mathcal{S}(k), \quad (35)$$

and is related to the angle-integrated spectrum by $\bar{E}_2(k) \propto k^{-1} \mathcal{E}_2(k)$ (see Equation B2). Therefore, reported power laws in literature are steeper by k^{-1} ^{133–135}.

The gray region in Figure 14(a) indicates the region where the point spread function (PSF) starts to dominate the spectral estimate. For the LMC, it has been acknowledged that apparent spectral breaks are caused by the PSF¹³³. The observed field $s_2^{\text{obs}}(\mathbf{x})$ is a convolution of the non-blurred field $s_2^{\text{true}}(\mathbf{x})$ with the PSF of the telescope $G_2^{\text{PSF}}(\mathbf{x})$ (we are

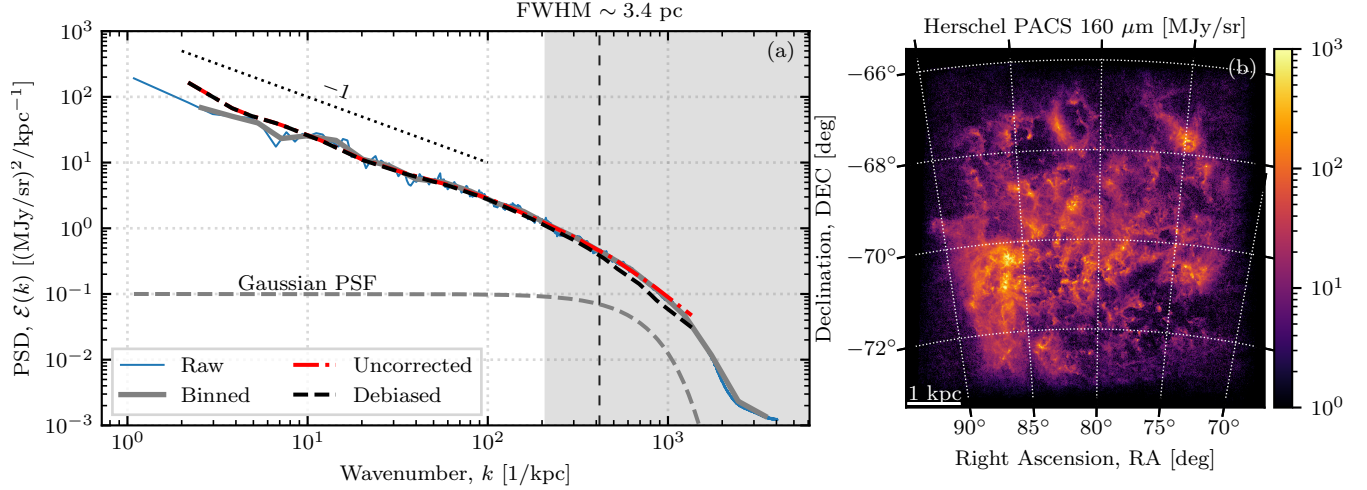


FIG. 14. Similar to Figure 13; (a) spatial PSD estimates of (b) Herschel PACS 160 μm observation of the Large Magellanic Cloud^{123,124}. The gray shaded region indicates where the effects of the limiting resolution of the data (the telescope’s point spread function) starts to influence the spectral estimates ($k \sim \frac{\sqrt{2}}{2 \times \text{FWHM}}$). Also showcasing the PSF influence, the gray dashed line shows a Gaussian approximation for the PSF normalized to an order of magnitude below unity. We have used $b = \sqrt{2}$.

ignoring the influence of noise),

$$s_2^{\text{obs}}(\mathbf{x}) = (s_2^{\text{true}} * G_2^{\text{PSF}})(\mathbf{x}). \quad (36)$$

Note that $s_2^{\text{true}}(\mathbf{x})$ is not necessarily the field that represents the system. *If* the system is 3D, then $s_2^{\text{true}}(\mathbf{x})$ is the corresponding projection (integration) along the line-of-sight and the observation, $s_2^{\text{obs}}(\mathbf{x})$, applies a convolution with the telescope PSF on top of the projection of the field. The spectral estimations we show represent the dataset. Conversion to the 3D system is non-trivial and requires further assumptions that are out-of-scope for this paper (see Section B 2 for more details).

The convolution theorem states that a convolution in real-space is multiplication in Fourier space,

$$E_2^{\text{obs}}(\mathbf{k}) = E_2^{\text{true}}(\mathbf{k}) E_2^{\text{PSF}}(\mathbf{k}). \quad (37)$$

where $E_2^{\text{true}}(\mathbf{k})$ is given by Equation B1. If we assume isotropy of all the spectra in Equation 37, by integrating both sides of Equation 37 over regions where $k = |\mathbf{k}|$,

$$\mathcal{E}_2^{\text{obs}}(k) = \mathcal{E}_2^{\text{true}}(k) \overline{E}_2^{\text{PSF}}(k), \quad (38)$$

where $E_2^{\text{PSF}}(k)$ is the angle-averaged spectrum (Equation 35) of the point-spread function and $\mathcal{E}_2^{\text{obs}}(k)$, $\mathcal{E}_2^{\text{true}}(k)$ are the observed and non-blurred angle-integrated spectra (Equation B2) respectively. Therefore, our observed PSD is a multiplication of the non-blurred angle-integrated spectra and the angle-averaged spectrum of the PSF. Modelling the PSF of the Herschel PACS $160\,\mu\text{m}$ band as a Gaussian with a full-width at half-maximum of $\approx 3.4\,\text{pc}^{136}$, we show $\overline{E}_2^{\text{PSF}}(k) = e^{-k^2\sigma^2}$ in (a) scaled to an order of magnitude below the amplitude for comparison purposes only. We do not retrieve $\mathcal{E}_D^{\text{true}}(k)$ in our analysis as the Gaussian PSF we use is not the true PSF present in the data^{123,136} and the process for obtaining $\mathcal{E}_D^{\text{true}}(k)$ is the same for $\tilde{\mathcal{E}}_D^S(k_e)$ as traditional $\mathcal{E}_D(k)$. See other spectral analysis literature for removing the influence of the PSF^{54,133}.

The “Uncorrected” slope at $k \gtrsim \sqrt{2}/(2 \times \text{FWHM})$ follows the “Binned” periodogram. The spectrum is steeper in this range resulting in a larger bias and therefore a “Debiased” slope that is smaller in amplitude at $k \gtrsim \sqrt{2}/\text{FWHM}$ than the “Binned” spectrum. The exponential-like roll-off in the (approximately Gaussian) PSF means the local power law debiasing technique might not be as effective. In this region, numerical noise for $\Delta\tilde{\beta}$ could also be strong, similar to Figure 12. This could explain the discrepancy between the “Debiased” and “Binned” curves.

The “Uncorrected” and “Debiased” PSD estimates are similar where $k \lesssim \frac{\sqrt{2}}{2*\text{FWHM}}$ due to the $\sim k^{-1}$ power law behaviour which has small bias. The “Uncorrected”, and “Debiased” slopes are similar to the “Binned” periodogram estimate beyond the FWHM scale which means the same techniques for reducing the influence of the PSF could be applied to $\tilde{\mathcal{E}}_D^S(k_e)$ as $\mathcal{E}_D(k)$. The PSF effects on the spectrum are outside the scope of this paper.

C. Isotropic Hydrodynamic Simulations, $D = 3$

In the absence of any real observation of turbulence that spans an entire 3-dimensional domain, we resort to simulations. We use data from an available high-resolution (1024^3) 3-dimensional incompressible, homogeneous, isotropic hydrodynamic turbulent simulation¹³⁷. The simulation is a direct numerical simulation of turbulence in a triply periodic cube where the Navier-Stokes equations are solved for in an incompressible fluid using a deterministically forced and statistically steady pseudo-spectral code¹³⁸. We use a single snapshot – `hit.1024.06468.h5` – which corresponds to ≈ 13 integral time-scales. The turbulence is

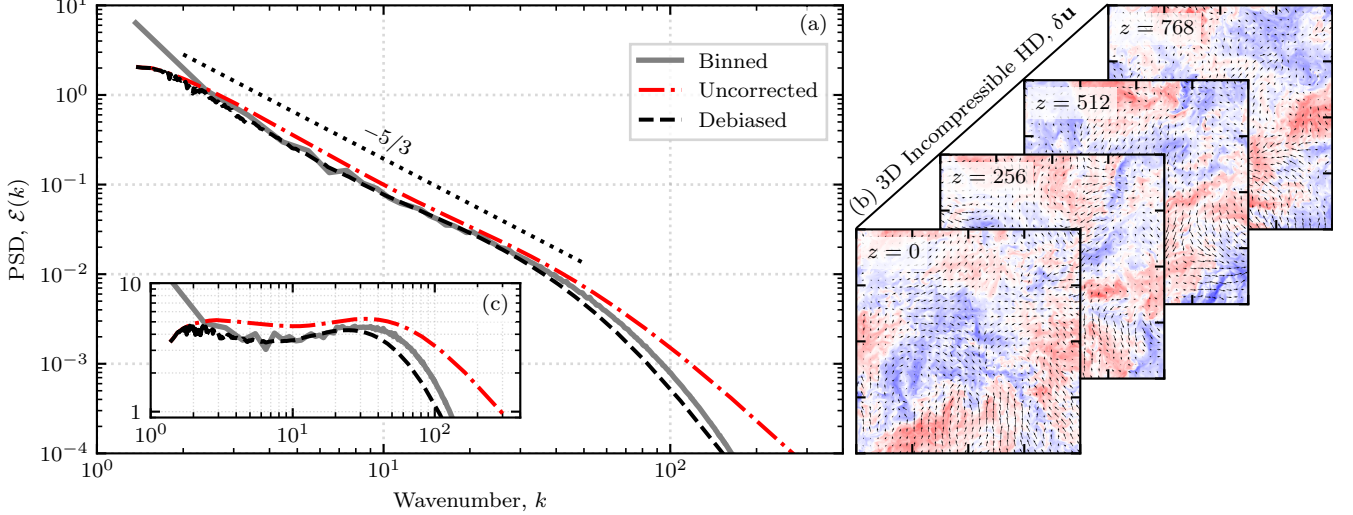


FIG. 15. Similar to Figure 13; (a) spatial PSD estimates of a 1024^3 3D incompressible hydrodynamic turbulence simulation¹³⁷ using $b = 2$. (b) z -slices of the simulation cube with the colour map representing δu_z from -7 (blue) to 7 (red) and the vector field representing $\delta u_x, \delta u_y$. (c) the same spectra shown in (a) but compensated by $k^{5/3}$. Axes scales are in code units.

fully developed.

To ease computations, we calculate the following parallel, and perpendicular structure functions using the simulation’s velocity field fluctuations $\delta \mathbf{u}(\mathbf{x}) = (\delta u_x(\mathbf{x}), \delta u_y(\mathbf{x}), \delta u_z(\mathbf{x}))$ (depicted in Figure 15(b)),

$$S_3^{\parallel,x}(\ell) = \langle |\delta u_x(\mathbf{x}) - \delta u_x(\mathbf{x} + \ell \hat{\mathbf{e}}_x)|^2 \rangle, \quad (39a)$$

$$S_3^{\perp,x}(\ell) = \langle |\delta u_y(\mathbf{x}) - \delta u_y(\mathbf{x} + \ell \hat{\mathbf{e}}_x)|^2 \rangle, \quad (39b)$$

$$\approx \langle |\delta u_z(\mathbf{x}) - \delta u_z(\mathbf{x} + \ell \hat{\mathbf{e}}_x)|^2 \rangle, \quad (39c)$$

to form $\bar{S}_3(\ell) = S_3^{\parallel,x}(\ell) + 2S_3^{\perp,x}(\ell)$. Note, Equation 39b and Equation 39c are equal only under perfect isotropy.

Since the simulation is incompressible, the zero-divergence condition required for this decomposition is met. The “Binned” $\mathcal{E}_D(k)$ (ground-truth) is calculated by integrating partial shells in the quadrant of positive k_x, k_y , with all of k_z . The resultant $\mathcal{E}_D(k)$ is multiplied by 4 to account for the missed quadrants for k_x, k_y . The PSD estimates using $b = 2$ ($b_{p,D}^{\text{est}}$) are shown in Figure 15(a).

A Kolmogorov $k^{-5/3}$ cascade region is present in the simulation. We see the $k^{-5/3}$ inertial range (power law slope) is captured well by $\tilde{\mathcal{E}}_D^S(k_e)$ (for both “Uncorrected” and “Debiased”

ased”). The “Uncorrected” curve has a larger amplitude in the inertial range ($3 \lesssim k \lesssim 20$) than $\mathcal{E}_D(k)$. This amplitude is appropriately corrected for in the “Debiased” curve as it almost exactly follows the “Binned” estimate. Due to the nature of the forcing in the simulation, there is no observed region with exponential growth (like that which was modelled in Section III D).

At larger k , the viscous term in the Navier-Stokes equation begins to dominate and results in an exponential roll-off in the spectrum^{139,140}. Towards the dissipation regime $k \gtrsim 60$, the “Uncorrected” estimate has a large bias and shows steepening of the curve, but not enough to describe the expected decay of the “Binned” $\mathcal{E}_D(k)$. At these large k , with steep decay curves, we would expect $\tilde{\mathcal{E}}_D^S(k_e) \sim k^{-3}$ corresponding to the steepest β possible for the equivalent spectrum (Section III A). This is also seen in the structure function^{20,57,141,142}. In a steep dissipation regime like $\mathcal{E}_D(k) \sim e^{-k/k_{\text{diss}}}$, $\Delta\tilde{\beta}$ will approach 3 for $k \gtrsim k_{\text{diss}}$. Since $\lim_{\beta \rightarrow 3^-} B_D^{\text{pow}}(\beta, b) = \infty$, using $\mathcal{B} = B_D^{\text{pow}}(\Delta\tilde{\beta}, b)$ will result in decay of $\mathcal{B}^{-1}\tilde{\mathcal{E}}_D^S(k_e)$ that is more rapid than the expected $e^{-k/k_{\text{diss}}}$. The accuracy of the “Debiased” $\mathcal{B}^{-1}\tilde{\mathcal{E}}_D^S(k_e)$ for steep dissipation regimes is not guaranteed. We see the “Debiased” $\mathcal{B}^{-1}\tilde{\mathcal{E}}_D^S(k_e)$ decays more rapidly than $\mathcal{E}_D(k)$ at $k \gtrsim 40$. At $k \gtrsim 100$, the “Uncorrected” curve has approached $\Delta\tilde{\beta} \approx 3$ and due to the clamping of $\Delta\tilde{\beta}$ (Section IV A), the “Debiased” curve will exhibit a constant power law behaviour.

Due to limited available bandwidth in the simulation, the $k^{-5/3}$ cascade region can be small¹⁴³. One such reason is the “bottleneck effect”: energy can pile-up in k -space around the dissipation scale k_{diss} ¹⁴⁴. This is evident in Figure 15(c) showing the compensated spectra $k^{5/3}\mathcal{E}_D(k)$, the pile-up starts around $k \gtrsim 20$. It has been shown that the scaling properties of $\bar{S}_D(\ell)$ and $\mathcal{E}_D(k)$ can be quite different in the bottleneck region^{80,145,146}. It has also been suggested that the second-order structure function is less sensitive to the bottleneck effect due to the non-local influence of the filter on $\mathcal{E}_D(k)$ in Equation 11¹⁴⁷. The bottleneck effect in the “Debiased” curve appears less pronounced in Figure 15(a). However, in (c) the shape of compensated spectrum for the “Debiased” curve is almost identical for $k > 3$ to the “Binned” $k^{5/3}\mathcal{E}_D(k)$ with just an apparent offset in equivalent wavenumber by $\approx 25\%$. Understanding the dynamics of the compensated equivalent spectrum (and other transformations on $\tilde{\mathcal{E}}_D^S(k_e)$) will be left for future work.

Overall, the “Uncorrected” curve shows that the equivalent spectrum must be debiased appropriately. In the case of a 3D incompressible hydrodynamic isotropic homogeneous sim-

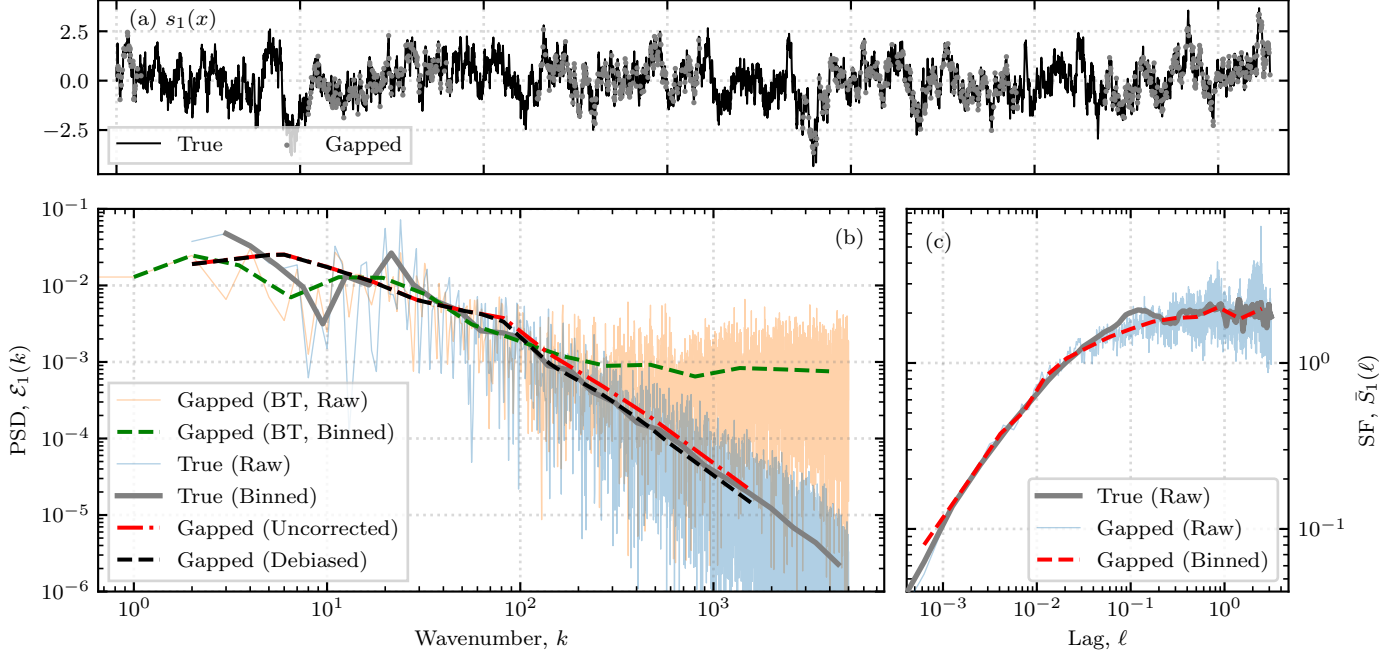


FIG. 16. (a) complete realization of a synthetic $D = 1$ fBm field (black) and a mock sparse/gapped sampling corresponding to $\approx 90\%$ missing data (gray dots). (b) PSD estimates on “Gapped” compared to the PSD estimates computed on the “True” fBm field (blue, and gray for the corresponding binned). (c) second order structure functions on the full data (gray) and on the gapped data (blue). The SF of the gapped data is binned to produce the smoothed SF estimate (red).

ulation, using $\mathcal{B} = B_D^{\text{pow}}$ with a local power law slope estimate $\Delta\tilde{\beta}$ results in an appropriate estimation of the PSD. The inertial range is shown in both the “Uncorrected” and “Debiased” curves as B_D^{pow} is small for $\beta \sim 5/3$ and $D = 3$. It is important to debias the equivalent spectrum since the “Uncorrected” curve looks like a broken power law spectrum of $\sim k^{-5/3}$ transitioning to $\sim k^{-3}$ at $k \gtrsim 60$. The “Debiased” curve is able to show dissipation-like behaviour beyond $k \gtrsim 60$. Although, it is unable to exactly match $\mathcal{E}_D(k)$.

D. Missing Data

One of the main strengths of this method is its application to datasets with missing data, which Fourier methods are well-known to struggle with. We plan to test this more exhaustively in future work, however here we show an initial test as proof of concept.

We test our method on sparse/gapped synthetic $D = 1$ fractional Brownian field (fBm)

data. We synthesize an fBm field of $N = 10000$ points in arbitrary units using the method described in Section IV B – this makes the “True” data which we compare the estimates to. We generate “Gapped” data by randomly removing large blocks, as well as randomly removing singular points of data from the “True”. We remove a total number of data points corresponding to $\approx 90\%$ missing data and $N = 1000$ points (shown in Figure 16(a)). From the “Gapped” and “True” dataset, we can compute the “True” PSD estimate, and estimates of the PSD using only the “Gapped” data.

In Figure 16(c), we compute the SF of the gapped data and compare it to the SF of “True”. The SF can be computed directly on the “Gapped” data where lag separations are available *i.e.*, values are based off pairs in the data, so if one or both values in a pair are missing, it can simply be ignored. It is recommended to apply corrections to “Gapped” SF estimations, however for our example we assume these corrections should be small since the field is Gaussian⁴⁹. At small ℓ , the SF shows the same power-law for both the “Gapped” and “True”. The “Gapped (Raw)” estimate is noisy at large scales which necessitates the binning procedure which we show as “Gapped (Binned)”. The “Gapped (Binned)” SF mostly follows the “True” SF except at scales $0.05 \lesssim \ell \lesssim 0.2$ – associated with the correlation scale of the synthesized fBm field. We use the “Gapped (Binned)” SF for computing $\tilde{\mathcal{E}}_D^S(k_e)$.

In Figure 16(b), we show the “Uncorrected” $\tilde{\mathcal{E}}_D^S(k_e)$ and “Debiased” $\mathcal{B}^{-1}\tilde{\mathcal{E}}_D^S(k_e)$ which corresponds to a PSD estimation solely from the ($\approx 90\%$) “Gapped” dataset. This constitutes a reasonable approximation of the “True (Binned)” (Periodogram) Fourier estimate on the full dataset. The ‘Debiased’ estimate follows the amplitude and slope in the power-law regime ($k \gtrsim 10^2$) as well as following the general trend of the “True (Binned)” PSD at $k \lesssim 10^2$.

For comparison of gapped PSD estimates, we include the Blackman-Tukey (BT) method³. The BT method estimates the PSD using the Fourier transform of an estimate for the autocorrelation function, hence, for the same reasons we can compute the structure function on the “Gapped” dataset, we can compute an estimate for the autocorrelation function on the “Gapped” dataset *i.e.*, only pairs of non-missing datapoints are considered. The BT method only exhibits similar behaviour to the “True” estimate at $k \lesssim 10^2$, the information at large k ($k \gtrsim 10^2$) is lost. The BT performs poorly as a PSD estimate in this range whereas the equivalent spectrum method is able to obtain the expected behaviour.

However, further work is required for quantifying the accuracy of $\tilde{\mathcal{E}}_D^S(k_e)$ on gapped data

of different types and where the data is non-Gaussian. Additionally, corrections to the estimation of the SF with gapped data should be considered in future work⁴⁹.

VI. CONCLUSION

We have introduced a method for estimating the angle-integrated power spectral density $\mathcal{E}_D(k)$ using the angle-averaged second-order structure function $\bar{S}_D(\ell)$: $\tilde{\mathcal{E}}_D^S(k_e)$ (Equation 8). We have thoroughly validated $\tilde{\mathcal{E}}_D^S(k_e)$ as a PSD estimate through a range of analytical and numerical techniques. With generalizations for dimension and power law of the data, we make the technique applicable to a wide range of fields and turbulence regimes.

Through $\tilde{\mathcal{E}}_D^S(k_e)$, we are able to investigate the relationship between Fourier wavenumber k and lag/physical-scale ℓ through the parameter $b = k\ell$. Appropriate decisions on b rely on the structure of $\mathcal{E}_D(k)$, but we have provided estimated and empirical formulae that should be appropriate for many circumstances (Equation 27, Equation 30). These results shed some light on the range of b values employed in the literature^{34,68,71,72,75,77}.

The ratio in amplitude between the structure function-based estimate for the spectrum $\tilde{\mathcal{E}}_D^S(k_e)$ and the actual spectrum $\mathcal{E}_D(k)$, denoted \mathcal{B} , has also been investigated. We show that in most cases we are able to account for the differences. We have suggested techniques for reducing these effects. By modelling spectra analytically, or through fractional Brownian motion fields the appropriate \mathcal{B} -factor can be understood. We also propose a general purpose debiasing method by using the pure power law bias B_D^{pow} (Equation 14) with a local power law estimate $\Delta\tilde{\beta}$ (Equation 31) which works well on practical data, or where the expected power law is not well known. In some cases $\mathcal{B} \approx 1$ and this debiasing makes little difference; in other cases it makes a significant difference.

This paper relates previous literature usage of the power-law approximation of the equivalent spectrum Equation 32^{49,65–67} to Equation 8⁶⁸ in Section III E. We also develop an understanding of the systematic biases of the equivalent spectrum through \mathcal{B} which is previously unreported.

The behaviour of b and \mathcal{B} depending on the structure of $\mathcal{E}_D(k)$ has been discussed throughout Section III C.

Finally, we showcased use of the equivalent spectrum for 1-dimensional in-situ solar wind turbulence measurements, 2-dimensional dust surface density of the Large Magellanic Cloud,

and a 3-dimensional hydrodynamic turbulence simulation. We find good agreements with Fourier PSD, which is used as the ground truth.

We show an example of the equivalent spectrum performing with gapped and sparse data, but future work will require further investigation and quantification of the accuracy of the estimator. Another area of potential improvement is in improving the technique by reducing noise introduced from the numerical differentiation and our naive binning and interpolation routines. Improvements could be made for example, through *e.g.*, Kalman^{148,149}, Savitzky-Golay¹⁵⁰ or other filtering techniques^{85,151} and even semi-parametric profile fitting¹⁵².

Appendix A: Additional Analytical Solutions

Following existing analytical spectral models from literature²² with $D = 1$ and power law $1 < \beta < 3$,

$$\mathcal{E}_1(k) = \frac{2}{\pi} \left(\frac{A^2}{A^2 + k^2} \right)^{\beta/2}, \quad (\text{A1})$$

the equivalent spectrum is,

$$\begin{aligned} \mathcal{B}\tilde{\mathcal{E}}_1^S(k_e) = & \frac{C}{b} \left(\frac{Ab}{2k_e} \right)^{H+1} \left[\right. \\ & \frac{Ab}{k_e} I_{H-1} \left(\frac{Ab}{k_e} \right) - \frac{Ab}{k_e} I_{-(H-1)} \left(\frac{Ab}{k_e} \right) \\ & + \frac{Ab}{k_e} I_{H+1} \left(\frac{Ab}{k_e} \right) - \frac{Ab}{k_e} I_{-(H+1)} \left(\frac{Ab}{k_e} \right) \\ & \left. + 2HI_H \left(\frac{Ab}{k_e} \right) - 2HI_{-H} \left(\frac{Ab}{k_e} \right) \right], \end{aligned} \quad (\text{A2})$$

where $C = \frac{\sqrt{\pi}}{\sin(\pi H) \Gamma(H + \frac{1}{2})}$, $I_\nu(\cdot)$ is a modified Bessel function of the first kind of ν -th order, and $\beta = 1 + 2H$ for $0 < H < 1$. Whilst the term $\left(\frac{Ab}{2k_e} \right)^{H+1}$ does not have the correct behaviour (it is only $\sim k_e^{-H-1}$), the remaining $\sim k_e^{-H}$ term can be seen by expanding the series representation of the modified Bessel functions

$$I_\nu \left(\frac{Ab}{k_e} \right) = \sum_{m=0}^{\infty} \frac{1}{\Gamma(m+1) \Gamma(m+\nu+1)} \left(\frac{Ab}{2k_e} \right)^{2m+\nu}, \quad (\text{A3})$$

up to terms of $\mathcal{O}(k_e^{-1})$. For $k_e \gg 1/A$, the terms in the square brackets are dominated by $\sim k_e^{-H}$, which primarily stems from the above series representation of the term $2HI_H \left(\frac{Ab}{k_e} \right)$. This gives us the remaining term to match the expected power law behaviour of $\sim k_e^{-2H-1}$.

Appendix B: Dimensional Considerations

1. D -dimensional Spectra

We define the angle integrated spectrum $\mathcal{E}_D(k)$ by first defining the modal spectrum

$$E_D(\mathbf{k}) = \frac{1}{(2\pi)^D} \int_{-\infty}^{\infty} \langle s_D(\mathbf{x}) s_D(\mathbf{x} + \boldsymbol{\ell}) \rangle_{\mathbf{x}} e^{-i\mathbf{k}\cdot\boldsymbol{\ell}} d^D \boldsymbol{\ell}, \quad (\text{B1})$$

with $\langle \cdot \rangle_{\mathbf{x}}$ averaging over spatial coordinate \mathbf{x} only. The angle-integrated spectrum is then obtained by integrating over a spherical shell $\mathcal{S}(k)$ of radius $k = |\mathbf{k}|$,

$$\mathcal{E}_D(k) = \int E_D(\mathbf{k}) d\mathcal{S}(k), \quad (\text{B2})$$

where

$$\Omega_D = \frac{2\pi^{D/2}}{\Gamma(D/2)}, \quad (\text{B3})$$

is the surface of the unit-sphere in D -dimensions where $\Omega_1 = 2$, $\Omega_2 = 2\pi$, and $\Omega_3 = 4\pi$. The angle-integrated spectrum, $\mathcal{E}_D(k)$ can be expressed in terms of the angle-averaged autocorrelation function,

$$\mathcal{E}_D(k) = \frac{\Omega_D^2}{(2\pi)^D} \int_0^{\infty} \bar{R}_D(\ell) \mathcal{T}_D(k\ell) (k\ell)^{D-1} d\ell, \quad (\text{B4})$$

where

$$\mathcal{T}_D(x) = \frac{\Gamma(D/2) \mathcal{J}_{D/2-1}(x)}{(x/2)^{D/2-1}}, \quad (\text{B5})$$

encapsulates the angle-averaging/integration, and integral transformation process for $\bar{R}_D(\ell)$ and $\mathcal{E}_D(k)$. The functions $\Gamma(\cdot)$, and $\mathcal{J}_n(x)$ are the (complete) Gamma function and the Bessel function of the first kind of n -th order respectively. For common D values, we get the expected transforms^{1,57}: $\mathcal{T}_1(x) = \cos(x)$, $\mathcal{T}_2(x) = \mathcal{J}_0(x)$, and $\mathcal{T}_3(x) = \frac{\sin(x)}{x}$. In other words, $\mathcal{E}_D(k)$ is the appropriate D -dimensional Fourier transformation.

Note, our convention of $\mathcal{E}_D(k)$ is twice the usual turbulence defintion, *i.e.*, we have $\int_0^{\infty} \mathcal{E}_D(k) dk = \langle s_D(\mathbf{x})^2 \rangle$ and $\mathcal{E}_D(k) dk$ would be twice the energy per unit mass. It is a simple procedure to multiply the middle equation of Equation 5 by a factor of 2 and propagate to the below equations to obtain the usual turbulence theory convention.

2. Sliced and Projected Data

In a lot of practical cases, observations of phenomena are restricted to only 1D slices, 2D projections, or 2D slices. These restrict the type of spectrum we obtain and could introduce additional artefacts and aliasing to the spectral estimates.

In the case of the solar wind (Section V A), measurements are performed by sensors moving in relation to the plasma rest frame. These sensors generate a time-series of data: such as magnetic field measurements $\mathbf{b}(t)$. We can construct the structure function and autocorrelation functions as,

$$S(\tau) = \langle |\mathbf{b}(t) - \mathbf{b}(t + \tau)|^2 \rangle, \quad (\text{B6})$$

$$R(\tau) = \langle \mathbf{b}(t) \cdot \mathbf{b}(t + \tau) \rangle \quad (\text{B7})$$

where $\langle \cdot \rangle$ averages over t , $|\cdot|$ is the vector norm, and we assume stationarity. We can also Fourier analyze this data by applying the Fourier transform to $R_1(\tau)$, giving a PSD $\mathcal{P}(\omega)$ that depends on frequency. Following the steps in Section II, we see that,

$$\int_0^\infty \frac{dS(\tau)}{d\tau} d\tau = \int_0^\infty \mathcal{P}(\omega) d\omega, \quad (\text{B8})$$

leads to the following approximation⁶⁸

$$\frac{1}{2} \frac{1}{b} \tau^2 \frac{dS(\tau)}{d\tau} \approx \mathcal{B}\mathcal{P}(\omega). \quad (\text{B9})$$

By assuming that the bulk flow is sufficiently fast, the temporal variations of $\mathbf{b}(t)$ at a fixed location (≈ 1 au) can be interpreted as spatial variations by $\mathbf{x} = -\mathbf{U}t$ (Taylor's frozen-in hypothesis)^{21,153} where $U \approx 400$ km/s is the average bulk flow speed of the slow solar wind¹⁵⁴. Using Taylor's frozen-flow hypothesis, we can interpret the time/frequency functions, $S(\tau)$, $R(\tau)$, $\mathcal{P}(\omega)$, as (approximations to) spatial functions with the lag ℓ_1 in the direction of the bulk flow U ,

$$S_3(\ell_1 = -U\tau, 0, 0) \approx S(\tau), \quad (\text{B10})$$

$$R_3(\ell_1 = -U\tau, 0, 0) \approx R(\tau), \quad (\text{B11})$$

and the Fourier transform of $R_3(\ell_1, 0, 0)$ corresponds to the “reduced” spectrum⁴⁰,

$$E_{\text{red}}(k_1) = \int_{-\infty}^{\infty} \int_{-\infty}^{\infty} E(k_1, k_2, k_3) dk_2 dk_3. \quad (\text{B12})$$

$\overline{R}_3(\ell)$	$E_{\text{red}}(k_1)$	$\widetilde{\mathcal{E}}_{\text{red}}^S(k_{e,1})$
\overline{A}	\overline{A}	\overline{A}
$\frac{(3L - \ell) e^{-\ell/L}}{L}$	$\frac{2L}{\pi} (L^2 k_1^2 + 1)^{-1}$	$\frac{2b^2 e^{-\frac{b}{Lk_{e,1}}}}{Lk_{e,1}^2}$
$\frac{(3L^2 - \ell^2) e^{-\ell^2/L^2}}{L^2}$	$\frac{L}{\sqrt{\pi}} e^{-L^2 k_1^2/4}$	$2b^2 e^{-\frac{b^2}{L^2 k_{e,1}^2}}$

TABLE III. **Analytical solutions for reduced spectra using different model autocorrelation functions.** Shown are: the reduced spectra $E_{\text{red}}(k_1)$ and the equivalent structure function estimator $\widetilde{\mathcal{E}}_{\text{red}}^S(k_{e,1})$ using these different forms of the autocorrelation function $\overline{R}_3(\ell)$.

The exact association to the full spectrum requires careful consideration and further assumptions *e.g.*, whether the turbulence is restricted to 2D planes, or is fully 3D¹⁵⁵. However, assuming fully 3D isotropic turbulence, we obtain,

$$\widetilde{\mathcal{E}}_{\text{red}}^S(k_{e,1}) \equiv \frac{1}{2} \frac{1}{b} \ell_1^2 \frac{\partial S_3(\ell_1, 0, 0)}{\partial \ell_1} \approx \mathcal{B} E_{\text{red}}(k_1) \quad (\text{B13})$$

where $k_{e,1} = b/\ell_1$ is the equivalent wavenumber associated with k_1 .

From Equation B12, it is easy to see that there is a form of aliasing where $E_{\text{red}}(k_1)$ is the energy associated with all wavevectors that have the same k_1 component. For example, some model functions from Table II for $E_{\text{red}}(k_1)$ are shown in Table III. These functions are largest at $k_1 = 0$. We also show the associated $\widetilde{\mathcal{E}}_{\text{red}}^S(k_{e,1})$ in Table III and can see that $\widetilde{\mathcal{E}}_{\text{red}}^S(k_{e,1})$ has a peak not at the origin – $\widetilde{\mathcal{E}}_{\text{red}}^S(k_{e,1})$ does not appear to exhibit such aliasing as with $E_{\text{red}}(k_1)$ ^{75,156}. Nevertheless, as with Equation 8, we can investigate cases in which the approximation holds true for appropriate biases b and \mathcal{B} for a range of k_e .

Above, we see that a slice of data produces projections of the Fourier spectrum. Now, we look at projections of data which are common in astronomical observations of turbulence such as the interstellar medium (Section V B). For a 3D scalar field $s_3(x, y, z)$ the plane-of-sky (POS) observation $p(x, y)$ is the projection along the line-of-sight (LOS) z -axis,

$$p(x, y) = \int_{\text{LOS}} s_3(x, y, z) dz, \quad (\text{B14})$$

where we have assumed there are no additional emissivity or modulation factors inside the integrand. From the *projection-slice theorem*, the spectrum of $p(x, y)$ – the plane-of-sky spectrum $E_{\text{POS}}(k_x, k_y)$ – is proportional to a slice of the full 3D spectrum of $s_3(x, y, z)$ at LOS wavenumber $k_z = 0$,

$$E_{\text{POS}}(\mathbf{k}_2) \propto E_3(\mathbf{k}_2, k_z = 0), \quad (\text{B15})$$

where $\mathbf{k}_2 = (k_x, k_y)$. By integrating wavenumber shells $\kappa_2 = |\mathbf{k}_2|$ in the observed 2D Fourier plane (following Equation B2) we obtain $\mathcal{E}_{\text{POS}}(\kappa_2) \neq \mathcal{E}_3(k)$ where $\mathcal{E}_3(k)$ is the angle-integrated spectrum of $s_3(x, y, z)$.

We assume that $\tilde{\mathcal{E}}_D^S(k_e)$ approximates the angle-integrated Fourier spectrum that is computed on the *observed* data *i.e.*, $\mathcal{E}_{\text{POS}}(\kappa_2)$, $\mathcal{P}(\omega)$. Conversion from the observed spectrum to the spectrum representing the dynamics of the system, *e.g.*, $\mathcal{E}_3(k)$, is a separate problem altogether.

Appendix C: Relation to Signature Functions

We use the integrands of Equation 7 to motivate Equation 8. This, of course does not mean we assume point-wise equality of the integrands of Equation 7. If we wished to assume point-wise (approximate) equality of the integrands, an equivalent expression would be:

$$\frac{1}{2} \frac{1}{b} \ell^2 \int_0^\infty \delta(\ell - r) \frac{d\bar{S}_D(r)}{dr} dr \approx - \int_0^\infty \delta(k - k_e) \mathcal{E}_D(k) dk. \quad (\text{C1})$$

From $\frac{d\Theta(x)}{dx} = \delta(x)$, where $\Theta(x)$ is the Heaviside step-function, Equation C1 is

$$\frac{1}{2} \frac{1}{b} \ell^2 \frac{\partial}{\partial \ell} \int_0^\ell \frac{d\bar{S}_D(r)}{dr} dr \approx - \frac{\partial}{\partial k_e} \int_{k_e}^\infty \mathcal{E}_D(k) dk. \quad (\text{C2})$$

Intrinsic to the process in Equation C2 is the filtering:

$$\int_0^\ell \frac{d\bar{S}_D(r)}{dr} dr \approx \int_{k_e}^\infty \mathcal{E}_D(k) dk, \quad (\text{C3})$$

i.e., the assumption that the structure function is well approximated by the sum of energy of all wavenumbers $k \geq k_e$,

$$\bar{S}_D(\ell) \approx \int_{k_e}^\infty \mathcal{E}_D(k) dk. \quad (\text{C4})$$

In this sense, k_e could be referred to as a “cut-off wavenumber” rather than an “equivalent wavenumber”.

It is worth noting from Equation 11, that really, there are higher-order contributions to $\bar{S}_D(\ell)$ ⁷⁵, *e.g.*, ignoring order-unity constants and Taylor expanding $1 - \mathcal{T}_D(k\ell)$ for small k ,

$$\bar{S}_D(\ell) \approx \int_{k_e}^\infty \mathcal{E}_D(k) dk + \ell^2 \int_0^{k_e} k^2 \mathcal{E}_D(k) dk + \dots \quad (\text{C5})$$

In other words, $\bar{S}_D(\ell)$ is the sum of energy in scales $\leq \ell$ and the enstrophy in scales $\geq \ell$ (plus higher-order corrections). In Section III C, we see that $\tilde{\mathcal{E}}_D^S(k_e)$ is *not* described by filters with sharp cutoffs.

A similar branch of literature worth mentioning is the *signature function*^{72,73,75,79,156,157}, $\mathcal{V}(\ell)$, which is intended to describe the turbulent energy distribution in real, rather than k -space with the following requirements:

Requirement 1: $\mathcal{V}(\ell) \geq 0$,

Requirement 2: $\int_0^\infty \mathcal{V}(\ell) d\ell = \langle s_D(\mathbf{x})^2 \rangle$,

Requirement 3: for a random distribution of eddies of size $\sim \ell_e$, the corresponding $V(\ell)$ has a clear peak around $\ell \sim \ell_e$.

No function has been found to meet all of these requirements, so usually, Requirement 1 is relaxed to $\int_0^\ell \mathcal{V}(r) dr \geq 0$ ^{75,156}.

It has been noted that the relationship of the signature function to the angle-integrated spectrum is,

$$\ell \mathcal{V}(\ell) \approx [k \mathcal{E}_D(k)]_{k_e}. \quad (\text{C6})$$

which is similar to Equation 9 upon re-arranging, for $\mathcal{V}(\ell) = \frac{d\bar{S}_D(\ell)}{d\ell}$, $k_e = b/\ell$, and assuming $\mathcal{B} = 1$ (point-wise equality). The estimate, Equation C6, is poor when $\mathcal{E}_D(k)$ exhibits steep gradients – which often occur outside the turbulence inertial range – and facilitates in the proposed constraint of the valid region of $\eta \ll \ell \ll L_I$ where η is the Kolmogorov microscale and L_I is the integral scale⁷⁵. This remark is backed by examination of $\mathcal{V}(\ell)$ and how it represents models with energy-containing ranges (like Section III B and Section III D for $D = 3$)⁷⁵.

Our approach (see, Equation 9) does *not* assume point-wise equality: \mathcal{B} accounts for this. Practically, \mathcal{B} allows for corrections based on local gradients and (in the context of Equation C6) reduces the error in the approximation. This correction factor can be modelled in several ways: the first requiring additional *a priori* assumptions about the shape of $\mathcal{E}_D(k)$ (a parametric-style approach, *e.g.*, Equation 29), and another that assumes local power-law behaviour (a non-parametric style approach, Section III E). Of course, \mathcal{B} is not universally applicable, and is merely sought to reduce the error for some range of ℓ .

AUTHOR CONTRIBUTIONS

M.A.B. contributed formal analysis, investigation, methodology, software, visualization, writing – original draft

S.O. contributed methodology, supervision, writing - review & editing

T.N.P. contributed conceptualization, methodology, supervision, writing - review & editing

Y.C.P. contributed funding acquisition, methodology, supervision, writing - review & editing

ACKNOWLEDGMENTS

Research supported by the Marsden Fund Council from NZ Government funding, managed by Royal Society Te Apārangi (E4200).

We thank the following for making their datasets accessible: *Wind* MFI and 3DP instrument teams and NASA GSFC’s Space Physics Data Facility¹⁵⁸, Clark et al.^{123,128} for the LMC dataset, Cardesa et al.¹³⁷ for the incompressible hydrodynamic simulation.

The authors wish to acknowledge the use of Victoria University of Wellington’s High Performance Compute Cluster Rāpoi as part of this research.

The authors wish to acknowledge the use of New Zealand eScience Infrastructure (NeSI) high performance computing facilities as part of this research. New Zealand’s national facilities are provided by NeSI and funded jointly by NeSI’s collaborator institutions and through the Ministry of Business, Innovation & Employment’s Research Infrastructure programme.¹⁵⁹

We thank D. Wrench for providing additional manuscript review.

We thank the anonymous referees for helpful suggestions that have improved the presentation and quality of this paper.

REFERENCES

¹R. N. Bracewell, *The Fourier Transform and Its Applications* (1986).

²A. Schuster, “On the investigation of hidden periodicities with application to a supposed

26 day period of meteorological phenomena,” Terrestrial Magnetism (Journal of Geophysical Research) **3**, 13 (1898).

³R. B. Blackman, J. W. Tukey, and T. Teichmann, “The Measurement of Power Spectra,” Physics Today **13**, 52 (1960).

⁴J. T. VanderPlas, “Understanding the Lomb-Scargle Periodogram,” The Astrophysical Journal Supplement Series **236**, 16 (2018).

⁵P. Stoica and R. Moses, *Spectral Analysis of Signals* (Pearson Prentice Hall Upper Saddle River, NJ, 2005).

⁶P. Babu and P. Stoica, “Spectral analysis of nonuniformly sampled data – a review,” Digital Signal Processing **20**, 359–378 (2010).

⁷D. J. Thomson and C. L. Haley, “Spacing and shape of random peaks in non-parametric spectrum estimates,” Proc Math Phys Eng Sci **470**, 20140101 (2014).

⁸M. W. Maciejewski, H. Z. Qui, I. Rujan, M. Mobli, and J. C. Hoch, “Nonuniform sampling and spectral aliasing,” J Magn Reson **199**, 88–93 (2009).

⁹K. Hocke and N. Kämpfer, “Gap filling and noise reduction of unevenly sampled data by means of the Lomb-Scargle periodogram,” Atmospheric Chemistry and Physics **9**, 4197–4206 (2009).

¹⁰L. T. Smith-Boughner and C. G. Constable, “Spectral estimation for geophysical time-series with inconvenient gaps,” Geophys J Int **190**, 1404–1422 (2012).

¹¹C. Munteanu, C. Negrea, M. Echim, and K. Mursula, “Effect of data gaps: Comparison of different spectral analysis methods,” Annales Geophysicae **34**, 437–449 (2016).

¹²S. Jahanjooy, R. Nikrouz, and N. Mohammed, “A faster method to reconstruct seismic data using anti-leakage Fourier transform,” J Geophys Eng **13**, 86–95 (2016).

¹³M. Roelens, L. Eyer, N. Mowlavi, I. Lecoeur-Taïbi, L. Rimoldini, S. Blanco-Cuaresma, L. Palaversa, M. Süveges, J. Charnas, and T. Wevers, “Short time-scale variables in the Gaia era: Detection and characterization by structure function analysis,” Mon Not R Astron Soc **472**, 3230–3245 (2017).

¹⁴A. D. Chave, “A multitaper spectral estimator for time-series with missing data,” Geophys J Int **218**, 2165–2178 (2019).

¹⁵L. F. Burlaga, “Intermittent turbulence in the solar wind,” Journal of Geophysical Research **96**, 5847–5851 (1991).

¹⁶M. A. Oliver and R. Webster, “A tutorial guide to geostatistics: Computing and modelling

variograms and kriging,” *Catena* **113**, 56–69 (2014).

¹⁷M. A. Oliver and R. Webster, *Basic Steps in Geostatistics: The Variogram and Kriging*, SpringerBriefs in Agriculture (Springer International Publishing, Cham, 2015).

¹⁸S. Sadhukhan, S. Bhattacharya, and M. K. Verma, “fastSF: A parallel code for computing the structure functions of turbulence,” *Journal of Open Source Software* **6**, 2185 (2021).

¹⁹E. Gatuzz, R. Mohapatra, C. Federrath, J. S. Sanders, A. Liu, S. A. Walker, and C. Pinto, “Measuring the hot ICM velocity structure function using XMM-Newton observations,” (2023).

²⁰A. S. Monin and A. M. Iaglom, *Statistical Fluid Mechanics: Mechanics of Turbulence. Volume 2 /Revised and Enlarged Edition/* (1975).

²¹U. Frisch, *Turbulence. The Legacy of A.N. Kolmogorov* (1995).

²²S. B. Pope, *Turbulent Flows* (2000).

²³D. Emmanoulopoulos, I. M. McHardy, and P. Uttley, “On the use of structure functions to study blazar variability: Caveats and problems,” *Monthly Notices of the Royal Astronomical Society* **404**, 931–946 (2010).

²⁴A. Kolmogorov, “The Local Structure of Turbulence in Incompressible Viscous Fluid for Very Large Reynolds’ Numbers,” *Akademiiia Nauk SSSR Doklady* **30**, 301–305 (1941).

²⁵A. N. Kolmogorov, “Dissipation of Energy in the Locally Isotropic Turbulence,” *Proceedings: Mathematical and Physical Sciences* **434**, 15–17 (1991), 51981.

²⁶A. Lorke and A. Wüest, “Application of Coherent ADCP for Turbulence Measurements in the Bottom Boundary Layer,” *Journal of Atmospheric and Oceanic Technology* **22**, 1821–1828 (2005).

²⁷P. J. Wiles, T. P. Rippeth, J. H. Simpson, and P. J. Hendricks, “A novel technique for measuring the rate of turbulent dissipation in the marine environment,” *Geophysical Research Letters* **33** (2006), 10.1029/2006GL027050.

²⁸S. A. Cohn, “Radar Measurements of Turbulent Eddy Dissipation Rate in the Troposphere: A Comparison of Techniques,” *Journal of Atmospheric and Oceanic Technology* **12**, 85–95 (1995).

²⁹G. Wang, F. Yang, K. Wu, Y. Ma, C. Peng, T. Liu, and L.-P. Wang, “Estimation of the dissipation rate of turbulent kinetic energy: A review,” *Chemical Engineering Science* **229**, 116133 (2021).

³⁰C. M. Brunt and M. H. Heyer, “Interstellar Turbulence. I. Retrieval of Velocity Field

Statistics,” The Astrophysical Journal **566**, 276–288 (2002).

³¹S. Boldyrev, Å. Nordlund, and P. Padoan, “Scaling Relations of Supersonic Turbulence in Star-forming Molecular Clouds,” ApJ **573**, 678 (2002).

³²P. Padoan, S. Boldyrev, W. Langer, and Å. Nordlund, “Structure Function Scaling in the Taurus and Perseus Molecular Cloud Complexes,” ApJ **583**, 308 (2003).

³³C. M. Brunt, M. H. Heyer, E. Vázquez-Semadeni, and B. Pichardo, “Intrinsic, Observed, and Retrieved Properties of Interstellar Turbulence,” The Astrophysical Journal **595**, 824–841 (2003).

³⁴C. Federrath, R. S. Klessen, L. Iapichino, and J. R. Beattie, “The sonic scale of interstellar turbulence,” Nature Astronomy **5**, 365–371 (2021).

³⁵P. J. Coleman, Jr., “Turbulence, Viscosity, and Dissipation in the Solar-Wind Plasma,” The Astrophysical Journal **153**, 371 (1968).

³⁶W. H. Matthaeus and M. L. Goldstein, “Measurement of the rugged invariants of magnetohydrodynamic turbulence in the solar wind,” Journal of Geophysical Research **87**, 6011–6028 (1982).

³⁷E. Marsch, “Turbulence in the Solar Wind,” in *Reviews in Modern Astronomy*, edited by G. Klare (Springer, Berlin, Heidelberg, 1991) pp. 145–156.

³⁸C. Y. Tu and E. Marsch, “On the nature of compressive fluctuations in the solar wind,” Journal of Geophysical Research: Space Physics **99**, 21481–21509 (1994).

³⁹R. Bruno and V. Carbone, “The Solar Wind as a Turbulence Laboratory,” Living Reviews in Solar Physics **10**, 2 (2013).

⁴⁰S. Oughton, W. H. Matthaeus, M. Wan, and K. T. Osman, “Anisotropy in solar wind plasma turbulence,” Philosophical Transactions of the Royal Society A: Mathematical, Physical and Engineering Sciences **373**, 20140152 (2015).

⁴¹C. H. K. Chen, “Recent progress in astrophysical plasma turbulence from solar wind observations,” Journal of Plasma Physics **82**, 535820602 (2016).

⁴²D. Verscharen, K. G. Klein, and B. A. Maruca, “The multi-scale nature of the solar wind,” Living Rev Sol Phys **16**, 5 (2019).

⁴³C. W. Smith and B. J. Vasquez, “Driving and Dissipation of Solar-Wind Turbulence: What Is the Evidence?” Frontiers in Astronomy and Space Sciences **7**, 114 (2021).

⁴⁴F. Fraternali, L. Adhikari, H. Fichtner, T. K. Kim, J. Kleimann, S. Oughton, N. V. Pogorelov, V. Roytershteyn, C. W. Smith, A. V. Usmanov, G. P. Zank, and L. Zhao,

“Turbulence in the Outer Heliosphere,” *Space Science Reviews* **218**, 50 (2022).

⁴⁵L. Gallana, F. Fraternale, M. Iovieno, S. M. Fosson, E. Magli, M. Opher, J. D. Richardson, and D. Tordella, “Voyager 2 solar plasma and magnetic field spectral analysis for intermediate data sparsity,” *Journal of Geophysical Research: Space Physics* **121**, 3905–3919 (2016).

⁴⁶R. A. Burger and S. R. McKee, “Evaluation and analysis of Voyager 1 48-s resolution magnetic field data,” *Advances in Space Research* **71**, 4916–4922 (2023).

⁴⁷M. Dorseth, J. C. Perez, S. Bourouaine, J. C. Palacios, and N. E. Raouafi, “The low-frequency power spectrum of slow solar wind turbulence,” *A&A* **689**, A117 (2024).

⁴⁸F. Fraternale, N. V. Pogorelov, J. D. Richardson, and D. Tordella, “Magnetic Turbulence Spectra and Intermittency in the Heliosheath and in the Local Interstellar Medium,” *ApJ* **872**, 40 (2019).

⁴⁹D. Wrench and T. N. Parashar, “De-Biasing Structure Function Estimates From Sparse Time Series of the Solar Wind: A Data-Driven Approach,” (2024), arXiv:2412.10053 [astro-ph].

⁵⁰E. W. Koch, E. W. Rosolowsky, R. D. Boyden, B. Burkhardt, A. Ginsburg, J. L. Loeppky, and S. S. R. Offner, “TURBUSTAT: Turbulence Statistics in Python,” *The Astronomical Journal* **158**, 1 (2019).

⁵¹B. Burkhardt, “Diagnosing Turbulence in the Neutral and Molecular Interstellar Medium of Galaxies,” *PASP* **133**, 102001 (2021).

⁵²Y. Li, M.-L. Gendron-Marsolais, I. Zhuravleva, S. Xu, A. Simionescu, G. R. Tremblay, C. Lochhaas, G. L. Bryan, E. Quataert, N. W. Murray, A. Boselli, J. Hlavacek-Larrondo, Y. Zheng, M. Fossati, M. Li, E. Emsellem, M. Sarzi, L. Arzamasskiy, and E. T. Vishniac, “Direct Detection of Black Hole-driven Turbulence in the Centers of Galaxy Clusters,” *The Astrophysical Journal* **889**, L1 (2020).

⁵³S. Ganguly, Y. Li, V. Olivares, Y. Su, F. Combes, S. Prakash, S. Hamer, P. Guillard, and T. Ha, “The Nature of the Motions of Multiphase Filaments in the Centers of Galaxy Clusters,” (2023).

⁵⁴E. Churazov, A. Vikhlinin, I. Zhuravleva, A. Schekochihin, I. Parrish, R. Sunyaev, W. Forman, H. Böhringer, and S. Randall, “X-ray surface brightness and gas density fluctuations in the Coma cluster,” *Monthly Notices of the Royal Astronomical Society* **421**, 1123–1135 (2012).

⁵⁵I. Zhuravleva, E. Churazov, A. A. Schekochihin, S. W. Allen, A. Vikhlinin, and N. Werner, “Suppressed effective viscosity in the bulk intergalactic plasma,” *Nature Astronomy* **3**, 832–837 (2019).

⁵⁶C. E. Romero, M. Gaspari, G. Schellenberger, T. Bhandarkar, M. Devlin, S. R. Dicker, W. Forman, R. Khatri, R. Kraft, L. Di Mascolo, B. S. Mason, E. Moravec, T. Mroczkowski, P. Nulsen, J. Orlowski-Scherer, K. Perez Sarmiento, C. Sarazin, J. Sievers, and Y. Su, “Inferences from surface brightness fluctuations of Zwicky 3146 via the Sunyaev-Zeldovich effect and X-ray observations,” (2023).

⁵⁷J. Stutzki, F. Bensch, A. Heithausen, V. Ossenkopf, and M. Zielinsky, “On the fractal structure of molecular clouds,” *Astronomy and Astrophysics* **336**, 697–720 (1998).

⁵⁸F. Bensch, J. Stutzki, and V. Ossenkopf, “Quantification of molecular cloud structure using the Delta -variance,” *Astronomy and Astrophysics* **366**, 636–650 (2001).

⁵⁹V. Ossenkopf, M. Krips, and J. Stutzki, “Structure analysis of interstellar clouds. I. Improving the Δ -variance method,” *Astronomy and Astrophysics* **485**, 917–929 (2008).

⁶⁰P. Arévalo, E. Churazov, I. Zhuravleva, C. Hernández-Monteagudo, and M. Revnivtsev, “A Mexican hat with holes: Calculating low-resolution power spectra from data with gaps,” *Monthly Notices of the Royal Astronomical Society* **426**, 1793–1807 (2012).

⁶¹N. Clerc, E. Cucchetti, E. Pointecouteau, and P. Peille, “Towards mapping turbulence in the intra-cluster medium. I. Sample variance in spatially-resolved X-ray line diagnostics,” *Astronomy and Astrophysics* **629**, A143 (2019).

⁶²E. Cucchetti, N. Clerc, E. Pointecouteau, P. Peille, and F. Pajot, “Towards mapping turbulence in the intra-cluster medium. II. Measurement uncertainties in the estimation of structure functions,” *Astronomy and Astrophysics* **629**, A144 (2019).

⁶³Y. P. Jing, “Correcting for the Alias Effect When Measuring the Power Spectrum Using a Fast Fourier Transform,” *The Astrophysical Journal* **620**, 559–563 (2005).

⁶⁴M.-A. Delsuc and P. O’Connor, “The Fourier transform in analytical science,” *Nat Rev Methods Primers* **4**, 1–16 (2024).

⁶⁵A. Chasapis, W. H. Matthaeus, T. N. Parashar, S. A. Fuselier, B. A. Maruca, T. D. Phan, J. L. Burch, T. E. Moore, C. J. Pollock, D. J. Gershman, R. B. Torbert, C. T. Russell, and R. J. Strangeway, “High-resolution Statistics of Solar Wind Turbulence at Kinetic Scales Using the Magnetospheric Multiscale Mission,” *ApJL* **844**, L9 (2017).

⁶⁶T. N. Parashar, A. Chasapis, R. Bandyopadhyay, R. Chhiber, W. H. Matthaeus,

B. Maruca, M. A. Shay, J. L. Burch, T. E. Moore, B. L. Giles, D. J. Gershman, C. J. Pollock, R. B. Torbert, C. T. Russell, R. J. Strangeway, and V. Roytershteyn, “Kinetic Range Spectral Features of Cross Helicity Using the Magnetospheric Multiscale Spacecraft,” *Phys. Rev. Lett.* **121**, 265101 (2018).

⁶⁷R. Chhiber, A. Chasapis, R. Bandyopadhyay, T. N. Parashar, W. H. Matthaeus, B. A. Maruca, T. E. Moore, J. L. Burch, R. B. Torbert, C. T. Russell, O. Le Contel, M. R. Argall, D. Fischer, L. Mirioni, R. J. Strangeway, C. J. Pollock, B. L. Giles, and D. J. Gershman, “Higher-Order Turbulence Statistics in the Earth’s Magnetosheath and the Solar Wind Using Magnetospheric Multiscale Observations,” *Journal of Geophysical Research: Space Physics* **123**, 9941–9954 (2018).

⁶⁸P. Thephthong, P. Pongkitiwanichakul, D. Ruffolo, R. Kieokaew, R. Bandyopadhyay, W. H. Matthaeus, and T. N. Parashar, “Scale and Time Dependence of Alfvénicity in the Solar Wind as Observed by Parker Solar Probe,” (2023).

⁶⁹Y. X. Huang, F. G. Schmitt, Z. M. Lu, and Y. L. Liu, “Autocorrelation function of velocity increments time series in fully developed turbulence,” *EPL* **86**, 40010 (2009).

⁷⁰Y. X. Huang, F. G. Schmitt, Z. M. Lu, P. Fougairolles, Y. Gagne, and Y. L. Liu, “Second-order structure function in fully developed turbulence,” *Phys. Rev. E* **82**, 026319 (2010).

⁷¹J. Squire and P. F. Hopkins, “The distribution of density in supersonic turbulence,” *Monthly Notices of the Royal Astronomical Society* **471**, 3753–3767 (2017).

⁷²P. A. Davidson and B. R. Pearson, “Identifying Turbulent Energy Distributions in Real, Rather than Fourier, Space,” *Phys. Rev. Lett.* **95**, 214501 (2005).

⁷³F. Hamba, “Turbulent energy density and its transport equation in scale space,” *Physics of Fluids* **27**, 085108 (2015).

⁷⁴In our convention, there is a factor of 2π radian in the wavenumber: k and k_e are really the *angular* wavenumbers. Since b is a dimensionless constant, when converting b/ℓ to k_e there is also an implicit multiplication of 1 radian. As radians are really dimension-less, there is no real consequence other than resolving confusing perspectives regarding angular units.

⁷⁵P. Davidson, *Turbulence: An Introduction for Scientists and Engineers* (Oxford University Press, 2015).

⁷⁶H. Tennekes and J. L. Lumley, *First Course in Turbulence* (1972).

⁷⁷M. J. Colbrook, X. Ma, P. F. Hopkins, and J. Squire, “Scaling laws of passive-scalar

diffusion in the interstellar medium,” Monthly Notices of the Royal Astronomical Society **467**, 2421–2429 (2017).

⁷⁸A. Simionescu, J. ZuHone, I. Zhuravleva, E. Churazov, M. Gaspari, D. Nagai, N. Werner, E. Roediger, R. Canning, D. Eckert, L. Gu, and F. Paerels, “Constraining Gas Motions in the Intra-Cluster Medium,” Space Science Reviews **215**, 24 (2019).

⁷⁹A. A. Townsend, *The Structure of Turbulent Shear Flow /2nd Edition/* (1976).

⁸⁰D. A. Donzis and K. R. Sreenivasan, “The bottleneck effect and the Kolmogorov constant in isotropic turbulence,” Journal of Fluid Mechanics **657**, 171–188 (2010).

⁸¹R. Beals and J. Szmigelski, “Meijer G-Functions: A Gentle Introduction,” Notices Amer. Math. Soc. **60**, 866 (2013).

82

$$\tilde{\mathcal{E}}_D^S(k_e) = 2^{2-\beta} \pi^{D/2} k_0^\alpha b^{\beta-1} k_e^{-\beta} \mathcal{M}_{3,0}^{0,2} \left(\frac{\beta-1}{2}, 1 \left| \frac{\alpha}{2} \left| \frac{4}{b^2} \frac{k^2}{k_0^2} \right. \right. \right) \quad (C7)$$

⁸³Other literature⁶⁸ has a factor of 1/4 (instead of our 1/2) because they have normalized to the *one-sided* $\mathcal{E}_D(k)$ *i.e.*,

$$\frac{\langle s_D(\mathbf{x})^2 \rangle}{2} = \int_0^\infty \mathcal{E}_D(k) dk, \quad (C8)$$

alternatively, thought of as normalizing such that $\mathcal{E}_D(k) dk$ represents the energy-per-unit mass. When we use Equation 4 and Equation 5, which states

$$\langle s_D(\mathbf{x})^2 \rangle = \int_0^\infty \mathcal{E}_D(k) dk. \quad (C9)$$

which means that $\mathcal{E}_D(k) dk$ represents twice the energy-per-unit mass.

⁸⁴K. Ahnert and M. Abel, “Numerical differentiation of experimental data: Local versus global methods,” Computer Physics Communications **177**, 764–774 (2007).

⁸⁵F. Van Breugel, J. N. Kutz, and B. W. Brunton, “Numerical Differentiation of Noisy Data: A Unifying Multi-Objective Optimization Framework,” IEEE Access **8**, 196865–196877 (2020).

⁸⁶L. Dyrud, B. Krane, M. Oppenheim, H. L. Pécseli, J. Trulsen, and A. W. Wernik, “Structure functions and intermittency in ionospheric plasma turbulence,” Nonlinear Processes in Geophysics **15**, 847–862 (2008).

⁸⁷L. Bentkamp and M. Wilczek, “Temporal large-scale intermittency and its impact on the statistics of turbulence,” Journal of Fluid Mechanics **1004**, A12 (2025).

⁸⁸T. Dudok de Wit, “Can high-order moments be meaningfully estimated from experimental turbulence measurements?” *Physical Review E* **70**, 055302 (2004).

⁸⁹G. A. Wood, “Data smoothing and differentiation procedures in biomechanics,” *Exerc Sport Sci Rev* **10**, 308–362 (1982).

⁹⁰M. F. Barnsley, R. L. Devaney, B. B. Mandelbrot, H.-O. Peitgen, D. Saupe, and R. F. Voss, *The Science of Fractal Images*, edited by H.-O. Peitgen and D. Saupe (Springer, New York, NY, 1988).

⁹¹M. A. Miville-Deschénes, F. Levrier, and E. Falgarone, “On the Use of Fractional Brownian Motion Simulations to Determine the Three-dimensional Statistical Properties of Interstellar Gas,” *The Astrophysical Journal* **593**, 831–847 (2003).

⁹²A. Esquivel, A. Lazarian, D. Pogosyan, and J. Cho, “Velocity statistics from spectral line data: Effects of density-velocity correlations, magnetic field and shear,” *Monthly Notices of the Royal Astronomical Society* **342**, 325–336 (2003).

⁹³V. Ossenkopf, A. Esquivel, A. Lazarian, and J. Stutzki, “Interstellar cloud structure: The statistics of centroid velocities,” *Astronomy and Astrophysics*, Volume 452, Issue 1, June II 2006, pp.223-236 **452**, 223 (2006).

⁹⁴A. Chepurnov and A. Lazarian, “Turbulence Spectra from Doppler-Broadened Spectral Lines: Tests of the Velocity Channel Analysis and Velocity Coordinate Spectrum Techniques,” *The Astrophysical Journal* **693**, 1074–1083 (2009).

⁹⁵J. Roman-Duval, C. Federrath, C. Brunt, M. Heyer, J. Jackson, and R. S. Klessen, “The Turbulence Spectrum of Molecular Clouds in the Galactic Ring Survey: A Density-dependent Principal Component Analysis Calibration,” *The Astrophysical Journal* **740**, 120 (2011).

⁹⁶G. V. Panopoulou, I. Psaradaki, R. Skalidis, K. Tassis, and J. J. Andrews, “A closer look at the ‘characteristic’ width of molecular cloud filaments,” *Monthly Notices of the Royal Astronomical Society* **466**, 2529–2541 (2017).

⁹⁷M. L. Bates, A. P. Whitworth, and O. D. Lomax, “Characterizing lognormal fractional-Brownian-motion density fields with a convolutional neural network,” *Monthly Notices of the Royal Astronomical Society* **493**, 161–170 (2020).

⁹⁸C. Vogt and T. A. Enßlin, “A Bayesian view on Faraday rotation maps Seeing the magnetic power spectra in galaxy clusters,” *Astronomy and Astrophysics*, Volume 434, Issue 1, April IV 2005, pp.67-76 **434**, 67 (2005).

⁹⁹J. A. ZuHone, M. Markevitch, and I. Zhuravleva, “Mapping the Gas Turbulence in the Coma Cluster: Predictions for Astro-H,” *The Astrophysical Journal* **817**, 110 (2016).

¹⁰⁰K. H. Kiyani, K. T. Osman, and S. C. Chapman, “Dissipation and heating in solar wind turbulence: From the macro to the micro and back again,” *Philosophical Transactions of the Royal Society A: Mathematical, Physical and Engineering Sciences* **373**, 20140155 (2015).

¹⁰¹J. L. Burch, T. E. Moore, R. B. Torbert, and B. L. Giles, “Magnetospheric Multiscale Overview and Science Objectives,” *Space Sci Rev* **199**, 5–21 (2016).

¹⁰²L. B. Wilson III, A. L. Brosius, N. Gopalswamy, T. Nieves-Chinchilla, A. Szabo, K. Hurley, T. Phan, J. C. Kasper, N. Lugaz, I. G. Richardson, C. H. K. Chen, D. Verscharen, R. T. Wicks, and J. M. TenBarge, “A Quarter Century of Wind Spacecraft Discoveries,” *Reviews of Geophysics* **59**, e2020RG000714 (2021).

¹⁰³J. Wang, W. H. Matthaeus, R. Chhiber, S. Roy, R. A. Predata, F. Pecora, and Y. Yang, “\$1/f\$ Noise in the Heliosphere: A Target for PUNCH Science,” *Sol Phys* **299**, 169 (2024).

¹⁰⁴M. Dorseth, S. Bourouaine, and J. C. Perez, “On the 1/f Spectrum in Slow Solar Wind Turbulence: The Role of Alfvénicity,” *The Astrophysical Journal* **974**, L34 (2024).

¹⁰⁵M. A. Bishop, S. Oughton, T. N. Parashar, and Y. C. Perrott, “Constraining Solar Wind Transport Model Parameters Using Bayesian Analysis,” *ApJ* **979**, 211 (2025).

¹⁰⁶D. Wrench, T. N. Parashar, S. Oughton, K. de Lange, and M. Frean, “What is the Reynolds Number of the Solar Wind?” *ApJ* **961**, 182 (2024).

¹⁰⁷W. H. Matthaeus, S. Dasso, J. M. Weygand, L. J. Milano, C. W. Smith, and M. G. Kivelson, “Spatial Correlation of Solar-Wind Turbulence from Two-Point Measurements,” *Physical Review Letters* **95**, 231101 (2005).

¹⁰⁸M. E. Cuesta, T. N. Parashar, R. Chhiber, and W. H. Matthaeus, “Intermittency in the Expanding Solar Wind: Observations from Parker Solar Probe (0.16 au), Helios 1 (0.3–1 au), and Voyager 1 (1–10 au),” *ApJS* **259**, 23 (2022).

¹⁰⁹J. A. Tesselin, C. W. Smith, B. T. MacBride, W. H. Matthaeus, M. A. Forman, and J. E. Borovsky, “Spectral Indices for Multi-Dimensional Interplanetary Turbulence at 1 AU,” *ApJ* **692**, 684 (2009).

¹¹⁰S. Boldyrev, J. Carlos Perez, J. E. Borovsky, and J. J. Podesta, “Spectral Scaling Laws in Magnetohydrodynamic Turbulence Simulations and in the Solar Wind,” *ApJL* **741**, L19 (2011).

¹¹¹T. S. Horbury, M. Forman, and S. Oughton, “Anisotropic Scaling of Magnetohydrodynamic Turbulence,” *Phys. Rev. Lett.* **101**, 175005 (2008).

¹¹²C. H. K. Chen, L. Leung, S. Boldyrev, B. A. Maruca, and S. D. Bale, “Ion-scale spectral break of solar wind turbulence at high and low beta,” *Geophysical Research Letters* **41**, 8081–8088 (2014).

¹¹³L. Franci, S. Landi, L. Matteini, A. Verdini, and P. Hellinger, “Plasma Beta Dependence of the Ion-scale Spectral Break of Solar Wind Turbulence: High-resolution 2D Hybrid Simulations,” *The Astrophysical Journal* **833**, 91 (2016).

¹¹⁴X. Wang, C. Y. Tu, J. S. He, and L. H. Wang, “Ion-Scale Spectral Break in the Normal Plasma Beta Range in the Solar Wind Turbulence,” *Journal of Geophysical Research (Space Physics)* **123**, 68–75 (2018).

¹¹⁵E. Marsch, “Origin and evolution of the solar wind,” *Proceedings of the International Astronomical Union* **2**, 259–268 (2006).

¹¹⁶B. G. Elmegreen and J. Scalo, “Interstellar Turbulence I: Observations and Processes,” *Annual Review of Astronomy and Astrophysics* **42**, 211–273 (2004).

¹¹⁷I. A. Gerrard, C. Federrath, N. M. Pingel, N. M. McClure-Griffiths, A. Marchal, G. Joncas, S. E. Clark, S. Stanimirović, M.-Y. Lee, J. T. van Loon, J. Dickey, H. Dénes, Y. K. Ma, J. Dempsey, and C. Lynn, “A new method for spatially resolving the turbulence-driving mixture in the ISM with application to the Small Magellanic Cloud,” *Monthly Notices of the Royal Astronomical Society* **526**, 982–999 (2023).

¹¹⁸G. Efstathiou, “Myths and truths concerning estimation of power spectra: The case for a hybrid estimator,” *Monthly Notices of the Royal Astronomical Society* **349**, 603–626 (2004).

¹¹⁹R. M. Sullivan, L. T. Hergt, and D. Scott, “Methods for CMB Map Analysis,” *Research Notes of the American Astronomical Society* **9**, 43 (2025).

¹²⁰M. Livio and T. M. Brown, eds., *The Local Group as an Astrophysical Laboratory: Proceedings of the Space Telescope Science Institute Symposium, Held in Baltimore, Maryland May 5–8, 2003*, Space Telescope Science Institute Symposium Series (Cambridge University Press, Cambridge, 2006).

¹²¹T. Ruiz-Lara, C. Gallart, M. Monelli, D. Nidever, A. Dorta, Y. Choi, K. Olsen, G. Besla, E. J. Bernard, S. Cassisi, P. Massana, N. E. D. Noël, I. Pérez, V. Rusakov, M. R. L. Cioni, S. R. Majewski, R. P. van der Marel, D. Martínez-Delgado, A. Monachesi, L. Monteagudo,

R. R. Muñoz, G. S. Stringfellow, F. Surot, A. K. Vivas, A. R. Walker, and D. Zaritsky, “The Large Magellanic Cloud stellar content with SMASH. I. Assessing the stability of the Magellanic spiral arms,” *Astronomy and Astrophysics* **639**, L3 (2020).

¹²²D. O. Cook, D. A. Dale, B. D. Johnson, L. Van Zee, J. C. Lee, R. C. Kennicutt, D. Calzetti, S. M. Staudaher, and C. W. Engelbracht, “The Spitzer Local Volume Legacy (LVL) global optical photometry,” *Monthly Notices of the Royal Astronomical Society* **445**, 881–889 (2014).

¹²³C. J. R. Clark, J. C. Roman-Duval, K. D. Gordon, C. Bot, and M. W. L. Smith, “The Quest for the Missing Dust. I. Restoring Large-scale Emission in Herschel Maps of Local Group Galaxies,” *The Astrophysical Journal* **921**, 35 (2021).

¹²⁴C. J. R. Clark, J. C. Roman-Duval, K. D. Gordon, C. Bot, M. W. L. Smith, and L. M. Z. Hagen, “The Quest for the Missing Dust: New Herschel Maps of Local Group Galaxies (LMC, SMC, M31, M33) that Restore Previously-Missed Extended Emission, Along With SED-Fitting Results, Hydrogen Gas Maps, and Swift UV Observations,” (2022).

¹²⁵A. Poglitsch, C. Waelkens, N. Geis, H. Feuchtgruber, B. Vandenbussche, L. Rodriguez, O. Krause, E. Renotte, C. van Hoof, P. Saraceno, J. Cepa, F. Kerschbaum, P. Agnèse, B. Ali, B. Altieri, P. Andreani, J. L. Auguera, Z. Balog, L. Barl, O. H. Bauer, N. Belbachir, M. Benedettini, N. Billot, O. Boulade, H. Bischof, J. Blommaert, E. Callut, C. Cara, R. Cerulli, D. Cesarsky, A. Contursi, Y. Creten, W. De Meester, V. Doublier, E. Doumayrou, L. Duband, K. Exter, R. Genzel, J. M. Gillis, U. Grözinger, T. Henning, J. Herreros, R. Huygen, M. Inguscio, G. Jakob, C. Jamar, C. Jean, J. de Jong, R. Katterloher, C. Kiss, U. Klaas, D. Lemke, D. Lutz, S. Madden, B. Marquet, J. Martignac, A. Mazy, P. Merken, F. Montfort, L. Morbidelli, T. Müller, M. Nielbock, K. Okumura, R. Orfei, R. Ottensamer, S. Pezzuto, P. Popesso, J. Putzeys, S. Regibo, V. Reveret, P. Royer, M. Sauvage, J. Schreiber, J. Stegmaier, D. Schmitt, J. Schubert, E. Sturm, M. Thiel, G. Tofani, R. Vavrek, M. Wetzstein, E. Wieprecht, and E. Wiezorek, “The Photodetector Array Camera and Spectrometer (PACS) on the Herschel Space Observatory,” *Astronomy and Astrophysics* **518**, L2 (2010).

¹²⁶M. W. Werner, E. E. Becklin, I. Gatley, M. J. Ellis, A. R. Hyland, G. Robinson, and J. A. Thomas, “Far-infrared observations of Large Magellanic Cloud H II regions.” *Monthly Notices of the Royal Astronomical Society* **184**, 365–376 (1978).

¹²⁷K. D. Gordon, J. Roman-Duval, C. Bot, M. Meixner, B. Babler, J.-P. Bernard, A. Bolatto,

M. L. Boyer, G. C. Clayton, C. Engelbracht, Y. Fukui, M. Galametz, F. Galliano, S. Hony, A. Hughes, R. Indebetouw, F. P. Israel, K. Jameson, A. Kawamura, V. Lebouteiller, A. Li, S. C. Madden, M. Matsuura, K. Misselt, E. Montiel, K. Okumura, T. Onishi, P. Panuzzo, D. Paradis, M. Rubio, K. Sandstrom, M. Sauvage, J. Seale, M. Sewiło, K. Tchernyshyov, and R. Skibba, “Dust and Gas in the Magellanic Clouds from the HERITAGE Herschel Key Project. I. Dust Properties and Insights into the Origin of the Submillimeter Excess Emission,” *The Astrophysical Journal* **797**, 85 (2014).

¹²⁸C. J. R. Clark, J. C. Roman-Duval, K. D. Gordon, C. Bot, M. W. L. Smith, and L. M. Z. Hagen, “The Quest for the Missing Dust. II. Two Orders of Magnitude of Evolution in the Dust-to-gas Ratio Resolved within Local Group Galaxies,” *The Astrophysical Journal* **946**, 42 (2023).

¹²⁹J. W. Brault and O. R. White, “The Analysis and Restoration of Astronomical Data via the Fast Fourier Transform,” *Astronomy and Astrophysics* **13**, 169 (1971).

¹³⁰J. M. Dickey, N. M. McClure-Griffiths, S. Stanimirović, B. M. Gaensler, and A. J. Green, “Southern Galactic Plane Survey Measurements of the Spatial Power Spectrum of Interstellar H I in the Inner Galaxy,” *The Astrophysical Journal* **561**, 264–271 (2001).

¹³¹R. Khatri and M. Gaspari, “Thermal SZ fluctuations in the ICM: Probing turbulence and thermodynamics in Coma cluster with Planck,” *Monthly Notices of the Royal Astronomical Society* **463**, 655–669 (2016).

¹³²I. Zhuravleva, E. Churazov, A. A. Schekochihin, S. W. Allen, P. Arévalo, A. C. Fabian, W. R. Forman, J. S. Sanders, A. Simionescu, R. Sunyaev, A. Vikhlinin, and N. Werner, “Turbulent heating in galaxy clusters brightest in X-rays,” *Nature* **515**, 85–87 (2014).

¹³³E. W. Koch, I.-D. Chiang, D. Utomo, J. Chastenet, A. K. Leroy, E. W. Rosolowsky, and K. M. Sandstrom, “Spatial power spectra of dust across the Local Group: No constraint on disc scale height,” *Monthly Notices of the Royal Astronomical Society* **492**, 2663–2682 (2020).

¹³⁴B. G. Elmegreen, S. Kim, and L. Staveley-Smith, “A Fractal Analysis of the H I Emission from the Large Magellanic Cloud,” *The Astrophysical Journal* **548**, 749–769 (2001).

¹³⁵B. G. Elmegreen, D. M. Elmegreen, and S. N. Leitner, “A Turbulent Origin for Flocculent Spiral Structure in Galaxies,” *The Astrophysical Journal* **590**, 271–283 (2003).

¹³⁶G. Aniano, B. T. Draine, K. D. Gordon, and K. Sandstrom, “Common-Resolution Convolution Kernels for Space- and Ground-Based Telescopes,” *Publications of the Astro-*

nomical Society of the Pacific **123**, 1218 (2011).

¹³⁷J. I. Cardesa, A. Vela-Martín, and J. Jiménez, “The turbulent cascade in five dimensions,” *Science* **357**, 782–784 (2017).

¹³⁸S. A. Orszag and G. S. Patterson, “Numerical Simulation of Three-Dimensional Homogeneous Isotropic Turbulence,” *Phys. Rev. Lett.* **28**, 76–79 (1972).

¹³⁹C. Foias, O. Manley, and L. Sirovich, “Empirical and Stokes eigenfunctions and the far-dissipative turbulent spectrum,” *Physics of Fluids A: Fluid Dynamics* **2**, 464–467 (1990).

¹⁴⁰P. W. Terry, A. F. Almagri, G. Fiksel, C. B. Forest, D. R. Hatch, F. Jenko, M. D. Nornberg, S. C. Prager, K. Rahbarnia, Y. Ren, and J. S. Sarff, “Dissipation range turbulent cascades in plasmas,” *Physics of Plasmas* **19**, 055906 (2012).

¹⁴¹A. Lazarian and D. Pogosyan, “Studying Turbulence Using Doppler-broadened Lines: Velocity Coordinate Spectrum,” *The Astrophysical Journal* **652**, 1348–1365 (2006).

¹⁴²A. Lazarian and D. Pogosyan, “Studying Velocity Turbulence from Doppler-broadened Absorption Lines: Statistics of Optical Depth Fluctuations,” *The Astrophysical Journal* **686**, 350–362 (2008).

¹⁴³M. Wan, S. Oughton, S. Servidio, and W. H. Matthaeus, “On the accuracy of simulations of turbulence,” *Physics of Plasmas* **17**, 082308 (2010).

¹⁴⁴G. Falkovich, “Bottleneck phenomenon in developed turbulence,” *Physics of Fluids* **6**, 1411–1414 (1994).

¹⁴⁵D. Lohse and A. Müller-Groeling, “Bottleneck Effects in Turbulence: Scaling Phenomena in r versus p Space,” *Phys. Rev. Lett.* **74**, 1747–1750 (1995).

¹⁴⁶D. Lohse and A. Müller-Groeling, “Anisotropy and scaling corrections in turbulence,” *Phys. Rev. E* **54**, 395–405 (1996).

¹⁴⁷W. Dobler, N. E. L. Haugen, T. A. Yousef, and A. Brandenburg, “Bottleneck effect in three-dimensional turbulence simulations,” *Phys. Rev. E* **68**, 026304 (2003).

¹⁴⁸S. Särkkä, *Bayesian Filtering and Smoothing*, Institute of Mathematical Statistics Textbooks (Cambridge University Press, Cambridge, 2013).

¹⁴⁹Y. Kim, H. Bang, Y. Kim, and H. Bang, “Introduction to Kalman Filter and Its Applications,” in *Introduction and Implementations of the Kalman Filter* (IntechOpen, 2018).

¹⁵⁰P.-O. Persson and G. Strang, “Smoothing by Savitzky-Golay and Legendre Filters,” in *Mathematical Systems Theory in Biology, Communications, Computation, and Finance*, edited by J. Rosenthal and D. S. Gilliam (Springer, New York, NY, 2003) pp. 301–315.

¹⁵¹M. Schmid, D. Rath, and U. Diebold, “Why and How Savitzky–Golay Filters Should Be Replaced,” *ACS Meas. Sci. Au* **2**, 185–196 (2022).

¹⁵²K. Wang, Y. Perrott, R. Arnold, and D. Huijser, “A semi-parametric approach to fitting gas pressure profiles of galaxy clusters,” *EPJ Web Conf.* **293**, 00051 (2024).

¹⁵³M. K. Verma, “Taylor’s frozen-in hypothesis for magnetohydrodynamic turbulence and solar wind,” *Physics of Plasmas* **29**, 082902 (2022).

¹⁵⁴D. J. McComas, B. L. Barraclough, H. O. Funsten, J. T. Gosling, E. Santiago-Muñoz, R. M. Skoug, B. E. Goldstein, M. Neugebauer, P. Riley, and A. Balogh, “Solar wind observations over Ulysses’ first full polar orbit,” *Journal of Geophysical Research: Space Physics* **105**, 10419–10433 (2000).

¹⁵⁵R. W. Fredricks and F. V. Coroniti, “Ambiguities in the deduction of rest frame fluctuation spectrums from spectrums computed in moving frames,” *Journal of Geophysical Research (1896-1977)* **81**, 5591–5595 (1976).

¹⁵⁶K. Chola and P. Chakraborty, “Revisiting Townsend’s spatial energy-density function,” *Journal of Fluid Mechanics* **1016**, A12 (2025).

¹⁵⁷F. Hamba, “Turbulent energy density in scale space for inhomogeneous turbulence,” *Journal of Fluid Mechanics* **842**, 532–553 (2018).

¹⁵⁸<https://spdf.gsfc.nasa.gov/>.

¹⁵⁹<https://www.nesi.org.nz>.